High-Resolution 3D Printed Microfluidic Devices for Dielectrophoretic Manipulation of Proteins

by

Samira Mahmud

A Thesis Presented in Partial Fulfillment
of the Requirements for the Degree
Master of Science

Approved March 2024 by the
Graduate Supervisory Committee:

Alexandra Ros, Chair
Chad Borges
Jeremy Mills

ARIZONA STATE UNIVERSITY

May 2024

ABSTRACT

Insulator-based dielectrophoresis (iDEP) has attracted considerable attention due to its ability to precisely capture and manipulate nanoparticles and biomolecules. A distinctive approach for effective manipulation of nanometer-sized proteins employing iDEP technique by generating higher electric field ($\boldsymbol{E}$) and gradient ($\boldsymbol{\nabla E^2}$) in the iDEP microfluidic devices is delineated. Strategies to generate higher $\boldsymbol{\nabla E^2}$ in the iDEP devices were outlined using numerical simulations. Intriguingly, the numerical simulation results demonstrated that by decreasing the post-to-post gap in the iDEP microfluidic devices, the $\boldsymbol{\nabla E^2}$ was increased by ~12 fold. Furthermore, the inclusion of channel constrictions, such as rectangular constriction or curved constriction into the straight channel iDEP microfluidic device led to a significant increase in $\boldsymbol{\nabla E^2}$. In addition, the inclusion of rectangular constrictions in the straight channel iDEP microfluidic device resulted in a greater increase in $\boldsymbol{\nabla E^2}$ compared to the incorporation of curved constrictions in the same device. Moreover, the straight channel device with horizontal post-to-post gap of 20 µm and vertical post-to-post gap of 10 µm generated the lowest $\boldsymbol{\nabla E^2}$ and the $\boldsymbol{\nabla E^2}$ was uniform across the device. The rectangular constriction device with horizontal and vertical post-to-post gap of 5 µm generated the highest $\boldsymbol{\nabla E^2}$ and the $\boldsymbol{\nabla E^2}$ was non-uniform across the device. Subsequently, suitable candidate devices were fabricated using soft lithography as well as high resolution 3D printing and the DEP behavior of ferritin examined under various experimental conditions. Positive streaming DEP could be observed for ferritin at low frequency in the device generating the lowest $\boldsymbol{\nabla E^2}$, whereas at higher frequency of 10 kHz no DEP trapping characteristics were apparent in the same device. Importantly, in the device geometry resulting in the highest $\boldsymbol{\nabla E^2}$ at 10 kHz, labeled ferritin exhibited pDEP

trapping characteristics. This is an indication that the DEP force superseded diffusion and became the dominant force.

ACKNOWLEDGMENTS

I would like to express my gratitude to my supervisor Dr. Alexandra Ros for her valuable guidance and support throughout my journey. I would like to thank all the members of Roslab for all the help and support. It truly means a lot. Moreover, I would like to thank my graduate supervisory committee members Dr. Chad Borges and Dr. Jeremy Mills for their valuable time and advice.

TABLE OF CONTENTS

Page

CHAPTER Page

CHAPTER Page

LIST OF TABLES

Table Page

LIST OF FIGURES

Figure Page

CHAPTER 1

INTRODUCTION

The manipulation of bioparticles and biomolecules, including DNA, cells, bacteria, viruses, and proteins, is of great significance in the field of biomedical research which encompasses areas such as systems biology, biomarker identification, drug discovery and development, along with high-throughput protein analysis. Interestingly, biomedical research can be advanced by lab-on-a-chip or microfluidic devices[1]. Microfluidics involves the manipulation of small amounts of fluids, ranging from 10^{-9} to 10^{-18} liters within channels with dimensions of tens to hundreds of micrometers in size. It has emerged as a notable field of study. Interestingly, microfluidics has the prospective to influence a range of sectors, spanning from chemical synthesis and biological analysis to optics and information technology[2]. Recently, within the realm of microfluidics, there has been an evolution of techniques designed to manipulate bioparticles and biomolecules by their unique physical and chemical characteristics. Furthermore, active and passive methods are known to allow fluid and particle separation in a microfluidic device. Passive methods include several fluid mechanisms and internal forces such as hydrodynamic filtration, hydrophoretic filtration, lateral displacement and inertia forces[3] and active methods include techniques such as optical methods, acoustophoresis, magnetophoresis, and dielectrophoresis (DEP), which are widely utilized.[3,4,5,6,7]

Intriguingly, insulator-based dielectrophoresis (iDEP) has attracted considerable attention due to its ability to precisely capture and manipulate nanoparticles[4,5], nucleic acids, proteins[6], organelles[7], cells etc. The DEP characteristics of colloidal nanoparticles and cells have been well elucidated by several researchers in respect of a well-developed

classical dielectric theory. Furthermore, the theoretical framework was also extensively verified with experimental observations[8].

Interestingly, among biomolecules, the manipulation of proteins through the application of an external force holds paramount interest both for fundamental research and real-world applications. Fundamental research on proteins includes the study of novel theoretical models for dielectrophoretic manipulation, in addition the exploration of the dielectrophoretic characteristics of proteins. Consequently, real-world applications utilizing the dielectrophoretic manipulation of proteins involve the development of drug delivery systems and biosensors for medicine, as well as utilizing proteins in biomedical applications. However, there still remains an incomplete comprehension of the mechanisms involved in the dielectrophoretic manipulation of proteins, and a general theoretical model has yet to be found[8].

There is an established basic DEP theoretical model for describing the dielectrophoretic (DEP) force acting on a spherical particle with dielectric properties.[9] The DEP force is a force that is applied on a dielectric particle when it is placed in a non-uniform electric field.

The basic DEP theoretical model is not applicable for explaining the dielectrophoretic manipulation of proteins. Recently, Hölzel, Pethig[10],[11] Colburn and Matyushov[12] extensively examined the limitations of the existing 'classical' DEP theory when attempting to elucidate the experimental manipulation of proteins[7]. They agree that the forces required for dielectrophoretic trapping of proteins should about 10^{21} V^2/m^3 considering the classical theory. Nevertheless, in series of studies conducted by numerous researchers through the past two decades, it was emphasized that protein dielectrophoresis

could be conducted by utilizing significantly lower $\boldsymbol{\nabla E^2}$ than the value predicted by the classical DEP theory[7]. The reason behind this unanticipated observation is due to the fact that proteins are polypeptides with charged side chains surrounded by a hydration shell responsible for forming their permanent dipole moment[7]. The 'classical' DEP theory only addresses the induced dipole moment of proteins. However, the total dipole moment of the protein is the combination of both the permanent and induced dipole moments and in a DEP experiment, the total dipole moment must be considered[7]. Consequently, the polarizability of proteins amplifies by several orders of magnitude as compared to that predicted by the standard macroscopic theory and the required $\boldsymbol{\nabla E^2}$ for the manipulation of proteins through DEP may be significantly reduced[7].

The classical DEP theory currently only contemplates the induced dipole moment. Therefore, Hölzel and Pethig[9,13,14] have attempted to provide a simple empirical relationship for the scrutinization of protein DEP by reconciling both polarization mechanisms. Recently, there are some propitious advancements in this direction: Matyushov and coworkers[12,15] have formulated a theoretical model encompassing correlation between proteins and water dipole moments and this considers the interaction between the two dielectrics in a mixture which is unnoticed in classical DEP theory[7]. Interestingly, this theoretical model is combined with extensive molecular dynamic simulations that represented a noteworthy step toward a better comprehension of protein DEP[7].

Matyushov et al.[12,15] addressed the issue concerning the minimal $\boldsymbol{\nabla E^2}$ necessary for protein trapping. The estimated $\boldsymbol{\nabla E^2}$ required[10,14,12,16,17] is on the order of 10^{21} V^2/m^3 according to the CM polarization mechanism which considered the Clausius-Mossotti

factor of proteins. Nonetheless, various researchers[10,14,12,16,17] reported protein capture occurring at significantly lower $\boldsymbol{\nabla E^2}$, sometimes as low as 10^{12} V^2/m^3. Most recently, Colburn and Matyushov et. al.[12] provided a new theoretical model, based on a dipolar mechanism which considered the dipole moment of proteins, where the estimated $\boldsymbol{\nabla E^2}$ required for capturing proteins is on the order of 10^{17} V^2/m^3.[12]

Dielectrophoretic manipulation of proteins using iDEP microfluidic devices has presented numerous challenges due to the extremely high $\boldsymbol{\nabla E^2}$ are required to manipulate nm-sized proteins. Electrode based DEP (eDEP) is one potential approach to achieve high $\boldsymbol{\nabla E^2}$ in the microfluidic devices. However, eDEP can lead to significant challenges such as Joule heating, electrode disintegration, analyte damage, and bubbling. Furthermore, insulator-based DEP (iDEP) is another potential approach to achieve high $\boldsymbol{\nabla E^2}$ by creating nm-sized gaps or constrictions in the microfluidic device. Several researchers have reported nm-sized gaps or constrictions in the past to generate higher $\boldsymbol{\nabla E^2}$ in the microfluidic devices using electron beam lithography or focused ion beam milling[18]. However, these fabrication methods are often not suitable due to their complex and expensive fabrication steps, requiring highly skilled personnel and sophisticated instruments in cleanroom facilities[18,19,20].

Intriguingly, three-dimensional (3D) printing has gained notable attention in microfluidics due to its rapid prototyping capabilities[21]. 3D-printing is an additive manufacturing method[22]. 3D printing offers various advantages over conventional lithography techniques, including a one-step fabrication process, rapid adjustment of device features and high-throughput fabrication[23]. Due to advancements in the microfluidic field, 3D-printed microfluidic devices have found extensive applications in numerous

fields including chemistry, biology, organ printing and solid-phase extraction, among others[24]. Recently, there has been immense consideration on the 3D printing approach named two-photon polymerization (2PP) because of its exceptional high-resolution printing capability[21]. Due to the high spatial resolution facilitated by the 2PP technique, nm-gap posts and constrictions can be incorporated in the iDEP microfluidic devices.

In this study, the aim is to generate higher $\boldsymbol{\nabla E^2}$ in a high-resolution 3D printed iDEP microfluidic device fabricated by a 2PP polymerization-based 3D printing technique, and to investigate the dielectrophoretic manipulation of proteins within the low frequency range. Ferritin which is a complex of hydrous ferric oxide and apoferritin [25] is used as a model protein for this study. Ferritin is a nm-sized globular protein and is composed of 24 structurally homologous protein subunits[25]. Moreover, ferritin is a non-fluorescent protein, and it was labeled with a fluorescent dye, fluorescein isothiocyanate (FITC), to explore its DEP properties. Firstly, a numerical model was developed to illustrate a strategy for generating higher $\boldsymbol{\nabla E^2}$ in the iDEP microfluidic devices. Secondly, the fabrication of the 3D printed devices was accomplished based on the outcomes of the numerical modelling, utilizing a 2PP polymerization-based 3D printing technique. Thirdly, the size distribution and zeta potential (ζ) of the ferritin were characterized using dynamic light scattering (DLS). Finally, the dielectrophoretic behavior of ferritin was analyzed in the low-frequency regime, both in conventional iDEP microfluidic devices with lower $\boldsymbol{\nabla E^2}$ and in 3D printed iDEP microfluidic devices capable of generating extremely high $\boldsymbol{\nabla E^2}$.

CHAPTER 2

BACKGROUND AND THEORY

2.1 Microfabrication

Microfabrication is a method that employed integrated-circuit manufacturing technology parallel to specialized processes to produce objects in the micrometer range[26]. Interestingly, microfabrication approaches for microfluidic applications enclose a exclusive range of materials and methodologies, spanning from conventional techniques like photolithography to high-resolution techniques like 3D printing[27].

2.1.1 Photolithography

Over the decades photolithography technique has manifested itself to be a feasible approach for fabricating microdevices devices or three-dimensional structures. Importantly, polydimethylsiloxane (PDMS) based microfluidic devices which are also known as conventional microfluidic devices exceedingly fabricated using the photolithography technique.

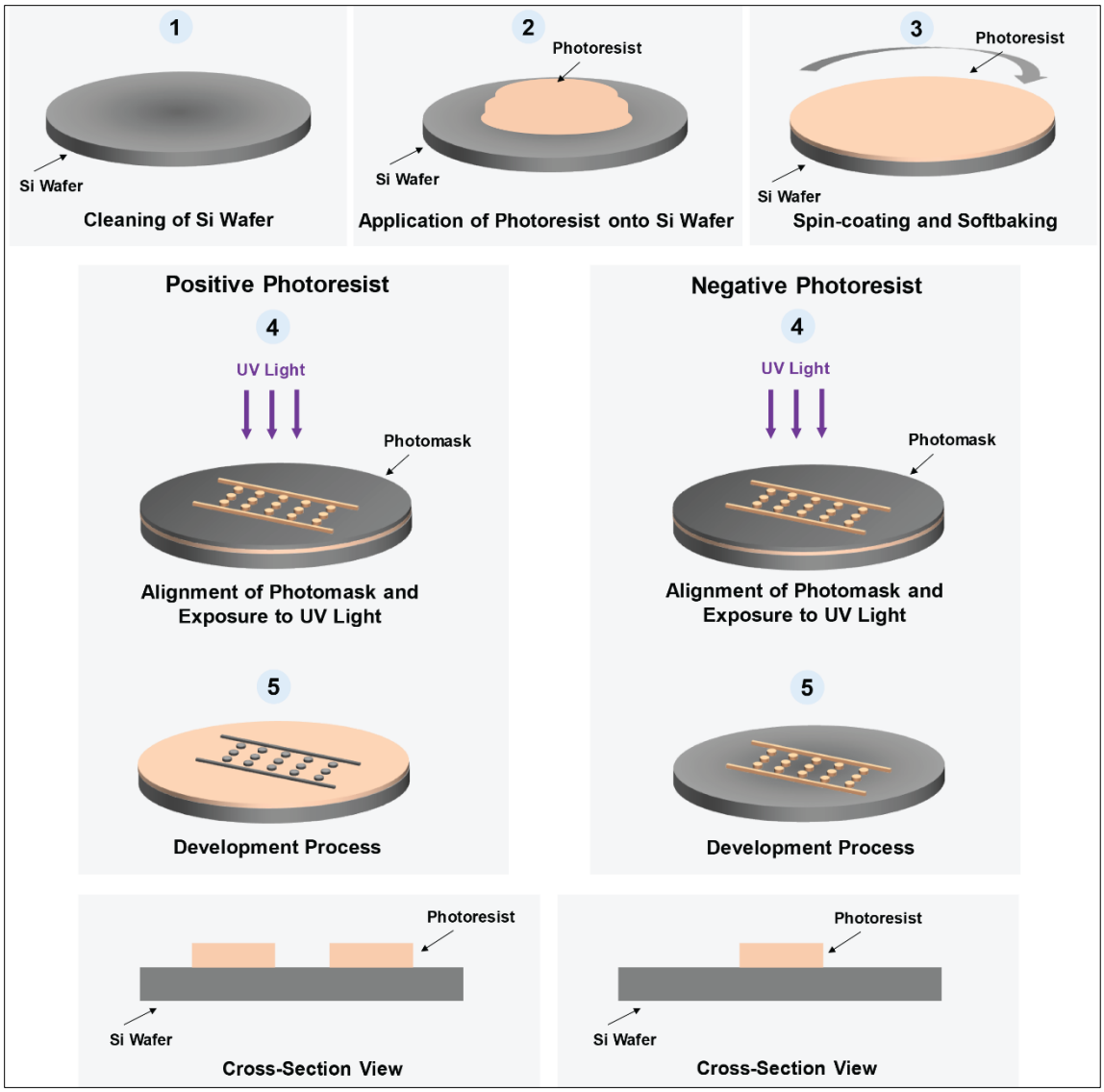

Figure 2.1: Schematic illustration of the main phases of the photolithographic process. (1) The Si wafer was properly cleaned using isopropyl alcohol, (2) the photosensitive polymer was poured on top of the substrate, (3) the photosensitive polymer was spin coated for precise control over the thickness, (4) UV exposure technique was used to transfer the pattern on the spin coated substrate and, (5) two types of the photoresists after development.

The primary steps of the photolithographic method are depicted in Figure 2.1.[28] Initially, the design of the microfluidic device are composed using a CAD software. Subsequently, the electron beam technique is utilized to produce the mask on the Si plates

to achieve precision at the micrometer scale. Afterward, a substrate made of silicon is taken and cleaned with isopropyl alcohol as depicted in Figure 2.1(1). The photosensitive polymer is poured on top of the substrate as depicted in Figure 2.1(2). Spin coating is employed to apply the photosensitive polymer onto the substrate, allowing for precise control over the thickness of the photosensitive material, as shown in Figure 2.1(3). Furthermore, to create a rigid layer prior to exposure to UV light, the wafer undergoes a soft baking process on a hot plate (not depicted). Subsequently, the pattern is transferred on the spin-coated substrate through mask alignment and exposure to a UV system as depicted in Figure 2.1(4). Upon completion of the exposure, the wafer is developed to eliminate any excess or undeveloped photoresist. Moreover, the wafer may undergo a hard-baking process (e.g., post-exposure bake) to achieve the desired design features on the master wafer.

Two varieties of photoresists exist: positive and negative. In positive photoresists the illuminated area becomes soluble after exposure, leaving the non-illuminated area insoluble during development. Consequently, the master wafer precisely replicates the pattern of the mask as demonstrated in Figure 2.1(5). Conversely, in negative photoresists, the photoresist polymerizes under exposure, and the developer solely eliminates the unexposed area. Consequently, the master wafer retains the inverse of the mask pattern as demonstrated in Figure 2.1(5).

Soft lithography involves producing microdevices or three-dimensional structures through molding and imprinting an elastomer onto a mold. Poly(dimethylsiloxane) (PDMS) is known as the most frequently utilized commercial elastomers for soft lithography.

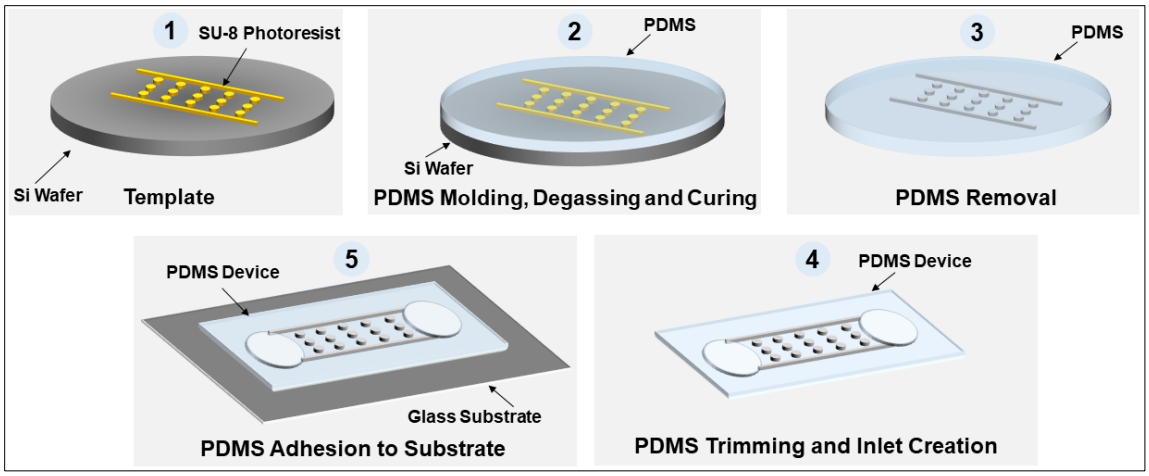

Figure 2.2: Schematic illustration of the steps of the fabrication of a PDMS device using soft-lithographic process. (1) A silicon wafer with SU-8 photoresist structures is prepared, (2) PDMS is poured on top of the silicon wafer, (3) After degassing and curing steps, PDMS slab is released from the master wafer, (4) The PDMS slab is cut into appropriate size and the two inlets are created, and (5) PDMS slab is attached on top of the glass substrate.

The method for producing PDMS microfluidic devices is depicted in Figure 2.2. Initially, a silicon rubber base, containing a copolymer of vinyl-terminated methylhydrosiloxane and dimethylsiloxane, is mixed with a curing agent at a ratio of 10:1. In Figure 2.2(1), a fabricated master with SU-8 structures is demonstrated. As demonstrated in Figure 2.2(2), PDMS liquid mixture is poured on top of the fabricated master with SU-8 structure. Following that, the PDMS slab is detached from the silicon wafer, as shown in Figure 2.2(3). The PDMS slab is trimmed into appropriate pieces and the two reservoirs are created using the puncture as depicted in Figure 2.2(4). Finally, the PDMS slab is bonded on top of the glass substrate through plasma oxidation as demonstrated in Figure 2.2(5).

2.1.2 High Resolution Three-Dimensional (3D) Printing

Three-dimensional (3D) printing employing two-photon polymerization (2PP) is an advanced technique in ultra-precise 3D microfabrication and nanofabrication. 2PP is a nonlinear optical process based on the two-photon absorption (TPA) theory[29].

In one-photon absorption (OPA), a molecule transitions from its ground energy state to a higher state via the absorption of one photon as demonstrated in Figure 2.3(a). OPA is a linear process where the absorbed energy correlates directly with the intensity of light.[28] In TPA, a molecule transitions from its ground energy state to a higher state via the simultaneous absorption of two photons, which may have different or equal frequencies as demonstrated in Figure 2.3(b). TPA is non-linear where the absorption is proportional to the square of the light intensity.[28]

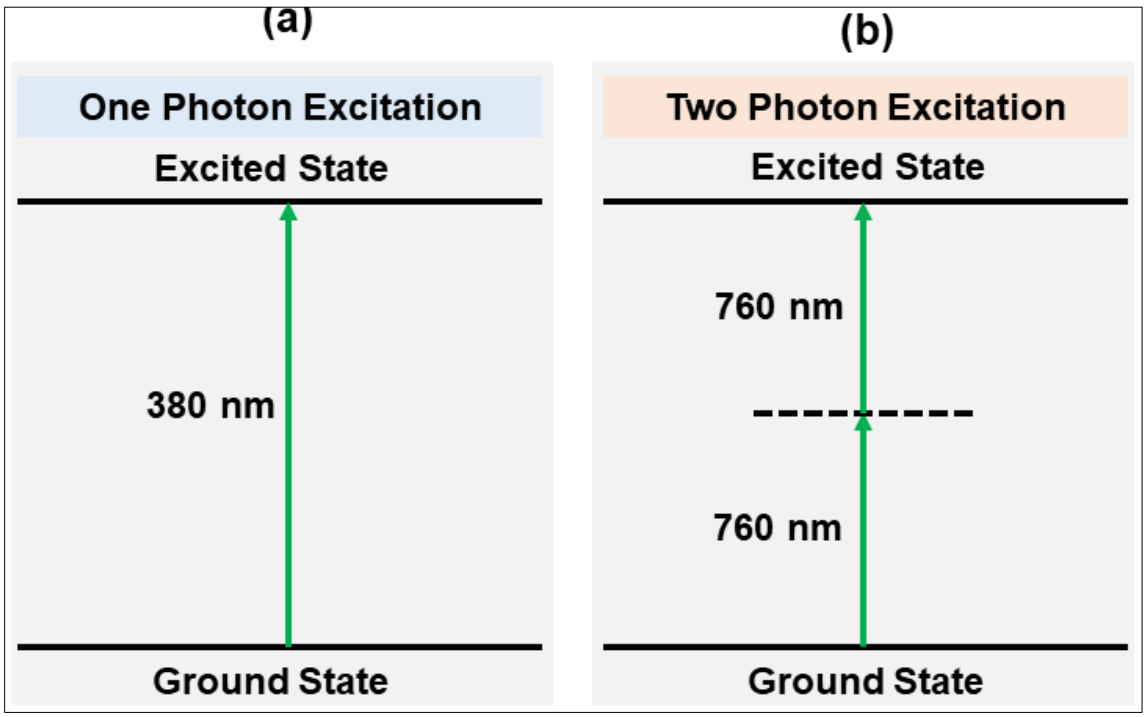

Figure 2.3: Schematic illustration of the contrast between the absorption energy of the excitation of (a) a single photon and (b) two photons.

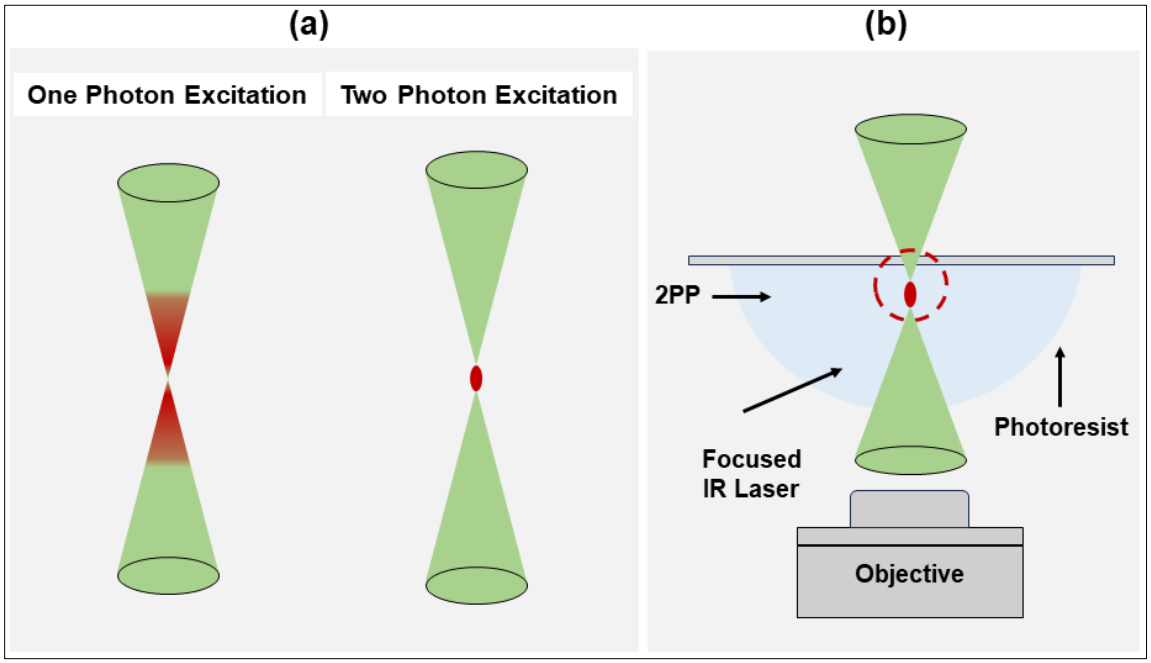

Figure 2.4: (a) Schematic illustration of the comparison of the excitation volume between one photon excitation where excitation occurs along the trace of the beam and two photon excitations where excitation is limited to the voxel around the focal point and, (b) Schematic illustration of the 3D printing process using the two-photon polymerization technique.

2PP is a nonlinear optical process that enables the excitation of the photons precisely concentrate on a point which generates the smallest unit of the 3D construction called a volume pixel (voxel). This voxel serves as the basis for fabricating the nano/micro 3D structure. In OPA, excitation takes place along a large portion of the focal volume, while in TPA, excitation is confined to the voxel surrounding the focal point[29] as depicted in Figure 2.4(a). The photosensitive material utilized in 2PP consists of acrylic-based resins, comprising a photo-initiator (PI) along with a blend of monomers and oligomers[29].

2PP technique is also known as direct laser writing (DLW), dip-in laser lithography (DiLL), or 3D laser lithography. Moreover, 2PP is a nonlinear optical process utilized the TPA theory[29, 30, 31]. Three-dimensional laser writing is accomplished by scanning a stage and employing a high-resolution objective lens. This objective focuses photons of 780 nm wavelength onto the photoresist and concentrates them into the voxel. [29, 30, 31] As demonstrated in Figures 2.3 and 2.4, the initial absorbed photon excites a single electron to a virtual state and then a second photon simultaneously excites the absorbed electron in the virtual state within a short time duration (~10^{-15} s). 2PP facilitates the achievement of high spatial resolution in the design of complicated 3D structures due to minimal two-photon absorption outside the focal point[30, 31].

2.2 Electrokinetic Phenomenon

Electrokinetic effects relate to the connection between the relative motion of two phases, generally a liquid phase and a solid phase, and the electrical characteristics of the interface between the two phases.

2.2.1 Electrophoresis

Electrophoresis is a phenomenon describing the movement of charged particles/ions comparative to the liquid it is suspended in under the influence of an electric field[32] as demonstrated in Figure 2.5. An electrophoretic setup comprises two electrodes applying a potential difference further connected through a conductive medium known as an electrolyte[32].

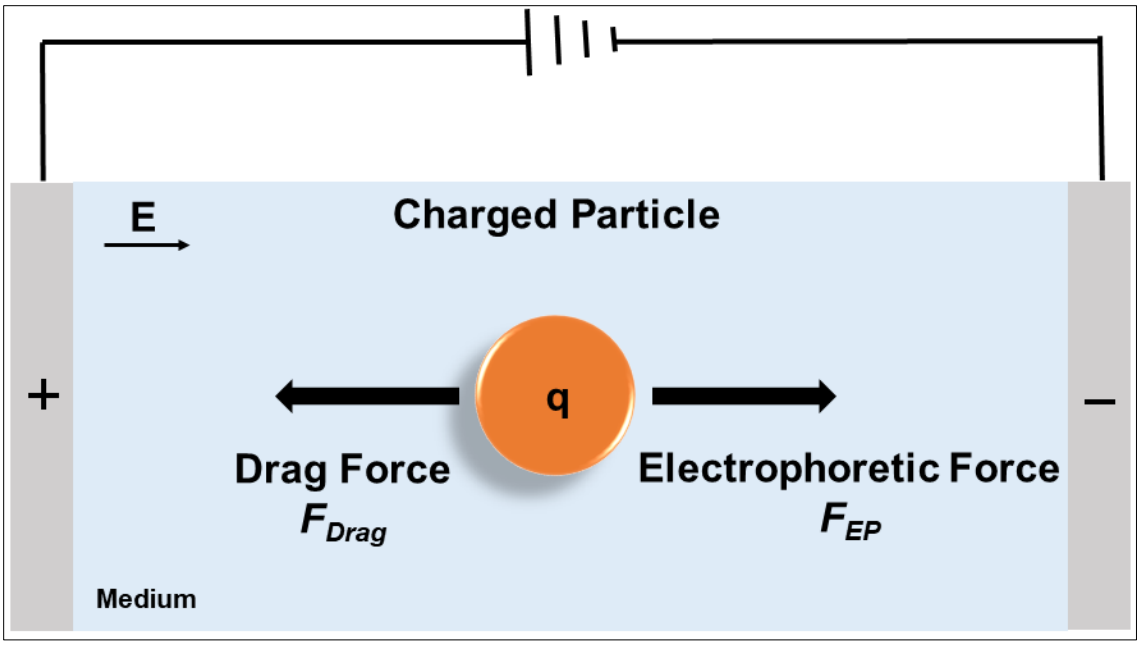

Figure 2.5: Schematic illustration of electrophoresis. The charged particle migrates under the influence of the electric field.

The electrophoretic force acting on the charged particles can be defined as[31, 32]:

$$\boldsymbol{F}_{ep} = q\boldsymbol{E} \qquad (2.2.1.1)$$

where $\boldsymbol{F}_{ep}$ is the electrophoretic for acting on the particle, q is the charge on the surface of the particle and $\boldsymbol{E}$ is the electric field strength.

The drag force, $\boldsymbol{F}_D$ acting on the particle which is based on the Stokes drag law can be expressed as[31, 32]:

$$\boldsymbol{F}_D = 6\pi\eta r\boldsymbol{\nu} \qquad (2.2.1.2)$$

where, $\boldsymbol{\nu}$ is the velocity of the particle, η is the mobility of the particle and r is the radius of the particle. The electrophoretic velocity $\boldsymbol{\nu}_{ep}$ can be derived when $\boldsymbol{F}_{ep}$ is balanced with $\boldsymbol{F}_D$:[31, 32]

$$6\pi\eta r\left(\mu - \boldsymbol{\nu}_{ep}\right) = q\boldsymbol{E} \qquad (2.2.1.3)$$

The electrophoretic mobility on the charged particles is defined as: [31, 32]

$$\mu_{ep} = \frac{\boldsymbol{v}_{ep}}{\boldsymbol{E}} = \frac{q}{6\pi\eta r} \qquad (2.2.1.4)$$

where $\boldsymbol{v}_{ep}$ is the electrophoretic velocity, μ_{ep} is the mobility of the particle. The electrophoretic mobility of a charged particle is dependent on the size of the particle, shape of the particle, and charges on the surface of the particle[33].

2.2.2 Electroosmosis

Electroosmosis is a phenomenon that involves the motion of liquid. The liquid is in close contact with a charged solid surface when an electric field is applied parallel to the surface[34] as demonstrated in Figure 2.6.

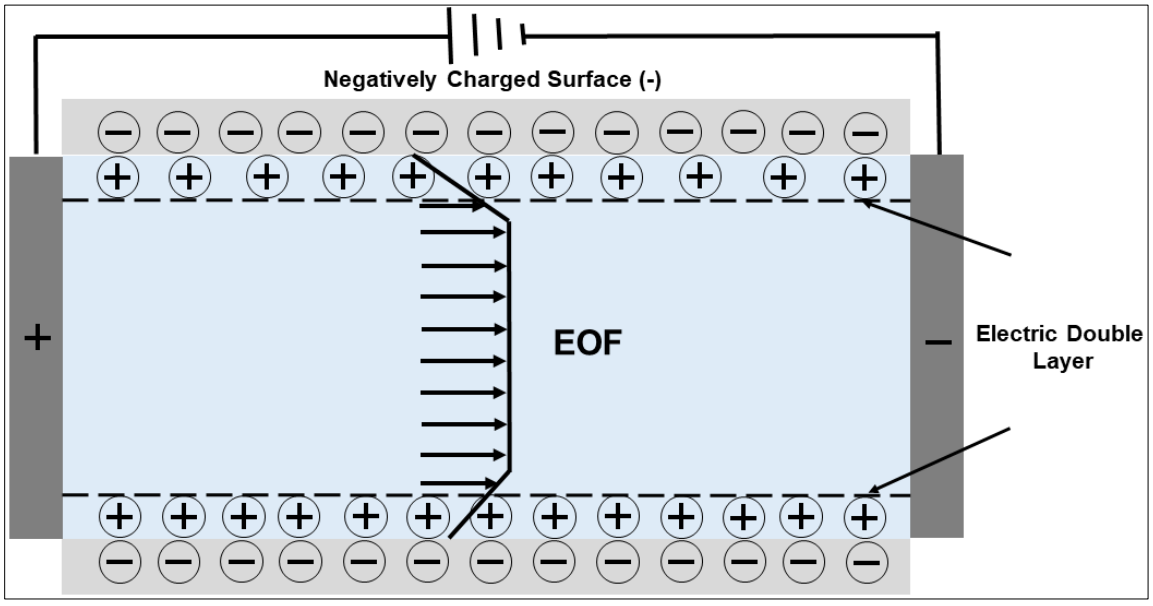

Figure 2.6: Schematic illustration of electroosmosis in a channel featuring negative surface charge. The EOF velocity remains consistent across the entire cross- section of the channel, reaching zero at the channel interface. The detailed charge distribution in the electrical double layer near the charged interface is omitted here for simplicity.

Many positive ions will be available in the surroundings of the liquid if the surface is negatively charged. Under the influence of the applied field, the excessive positive ions are expedited, and, in sequence, they draw the liquid along them. The electroosmotic velocity can be defined as[33]:

$$\boldsymbol{v}_{eo} = \mu_{eo}\boldsymbol{E} \qquad (3)$$

where, $\boldsymbol{v}_{eo}$ is the electroosmotic velocity and μ_{eo} is the electroosmotic mobility.

2.2.3 Dielectrophoresis

Dielectrophoresis (DEP) is an analytical method that describes the movement of a polarizable particle when subjected to a non-uniform electric field. Interestingly, DEP is influenced by both the dipole moment of the particle and spatial gradient of the electric field as demonstrated in Figure 2.7.[9, 35] The DEP responses of the components are dependent on the characteristics of the analytes, with paramount parameters including the conductivities and permittivities. Moreover, the size and shape of the analyte also prominently influences the DEP response. DEP is intrinsically a label-free technique, though significant labeling strategies may be required for enhanced sensitivity. Additionally, DEP has the potential to be a cost-effective diagnostic method and thus DEP offers several advantages compared to other analytical techniques.[9] Interestingly, there are different fundamental DEP theories for different shaped particles, beginning with spherical structured particles, advancing to more complicated structures like double-shell and multiple-shell spherical structured particles, and furthermore extending to particles with distinct non-spherical shapes[8].

A basic theoretical model of DEP to elucidate the DEP force exerted on a spherical colloidal particle exhibiting dielectric characteristics under the influence of a non-uniform electric field is given as[9]:

$$F_{DEP} = 2\pi r^3 \varepsilon_m Re(CM) \boldsymbol{\nabla} \boldsymbol{E}^2 \qquad (2.2.3.1)$$

where F_{DEP} is the DEP force experienced by the spherical colloidal particle, r is the radius of the analyte, ε_m is the relative permittivity of the surrounding medium, $Re(CM)$ is the real part of the Clausius-Mossotti function.

The DEP force exerted on a spherical colloidal particle relies on both the radius as well as the magnitude and sign of the Clausius-Mossotti factor (CM):

$$Re(CM) = \frac{\varepsilon_p^* - \varepsilon_m^*}{\varepsilon_p^* - 2\varepsilon_m^*} \qquad (2.2.3.2)$$

where, ε_p^* is the complex permittivity of the particle and ε_m^* is the complex permittivity of the medium with:

$$\varepsilon_p^* = \varepsilon_p - i\,\frac{\sigma_p}{\omega} \quad (2.2.3.3) \text{ and } \varepsilon_m^* = \varepsilon_m - i\,\frac{\sigma_m}{\omega} \quad (2.2.3.4)$$

Here, ε_p is the permittivity of the particle, ε_m is the permittivity of the medium, σ_p is the conductivity of the particle, σ_m is the conductivity of the medium and ω is the angular frequency.

When a suspended particle exhibits higher polarizability compared to the surrounding medium, it is moved towards the region of higher electric field, resulting in the accumulation of particles where the electric field reaches its maximum value; this phenomenon is referred to as positive DEP (pDEP)[8] as depicted in Figure 2.7(a). Moreover, when the polarizability of a suspended particle is lower compared to the surrounding medium, it is moved towards the region of lower electric field, resulting in the

accumulation of particles where the electric field reaches its minimum value; this phenomenon is referred to as negative DEP (nDEP)[8] as depicted in Figure 2.7(b). In simpler terms, spherical particles with $Re(CM) > 0$ experience pDEP and spherical particles with $Re(CM) < 0$ experience nDEP.[9]

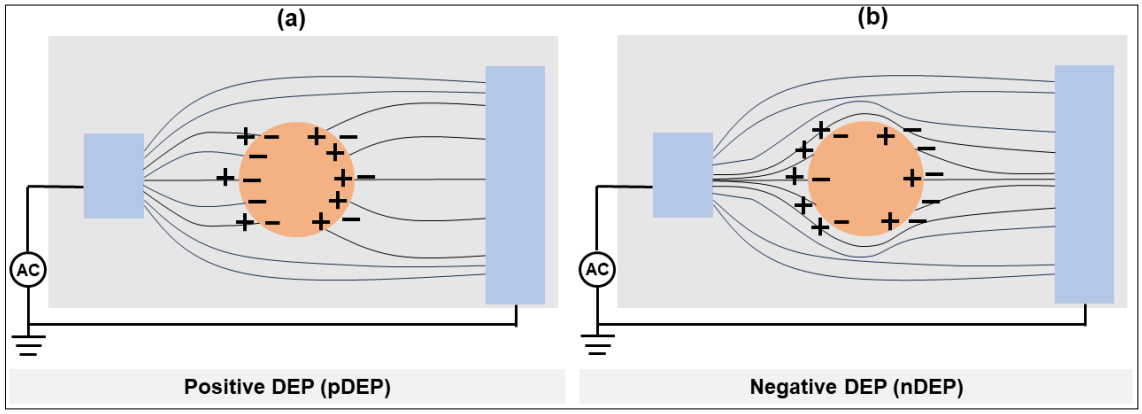

Figure 2.7: Schematic illustration of DEP of a spherical particle in a non-uniform electric field distribution. (a) When the particle conductivity is higher than the medium conductivity, the particle migrates toward the higher electric field, resulting in positive DEP and (b) when the medium conductivity is higher than the particle conductivity, the particle migrates toward the lower electric field, resulting in negative DEP. The black lines are represented the electric field lines.

As illustrated in Figure 2.1, when a dielectric particle is placed in the non-uniform electric field than it induces unequal Coulomb forces on the two poles of the induced dipole. As demonstrated in Figure 2.1(a), when the permittivity of the particle exceeds the permittivity of the surrounding medium, the overall force acting on the particle is directed toward intense field, leading to pDEP. Alternatively, as demonstrated in Figure 2.1(b), when the permittivity of the medium surpasses the permittivity of the particle, it encounters forces in the opposite direction, leading to nDEP.[9]

The equation of the real part of the Clausius-Mossotti factor is described in Equations 2.2.3.5[36].

$$Re(CM) = \frac{\omega^2 (\varepsilon_p - \varepsilon_m)(\varepsilon_p + 2\varepsilon_m) + (\sigma_p - \sigma_m)(\sigma_p + 2\sigma_m)}{\omega^2 (\varepsilon_p + 2\varepsilon_m)^2 + (\sigma_p + 2\sigma_m)^2} \qquad (2.2.3.5)$$

There are two limiting cases of the $Re(CM)$ which are described in the following Equations. The first limit is examined at low frequencies, offering the ionic contribution to the permittivity. It corresponds to the limit $\omega \to 0$ in the expression[36],

$$R_e[(CM)(\omega \to 0)] = \frac{(\sigma_p - \sigma_m)}{(\sigma_p + 2\sigma_m)} \qquad (2.2.3.6)$$

It can be easily verified that this limit turns positive when $\sigma_p > \sigma_m$ or this limit turns negative when $\sigma_p < \sigma_m$.[36] The second limit is examined at higher frequencies, providing the ionic contribution to the permittivity. This corresponds to the limit $\omega \to \infty$ in the expression[36],

$$R_e[(CM)(\omega \to \infty)] = \frac{(\varepsilon_p - \varepsilon_m)}{(\varepsilon_p + 2\varepsilon_m)} \qquad (2.2.3.7)$$

It can be easily verified that this limit turns negative when $\varepsilon_p > \varepsilon_m$ or this limit turns positive if $\varepsilon_p < \varepsilon_m$. [36]

2.2.4 Streaming Dielectrophoresis

Streaming dielectrophoresis (DEP) refers to the focusing of particles into streams by equilibrating the DEP force and the electrokinetic forces acting on the particles.[37, 38] The nature of streaming DEP flow within arrays is highly influenced by the shapes of the posts and the orientation of the array relative to the applied electric field. This characteristic makes such a system prone to engineering optimizations.[39]

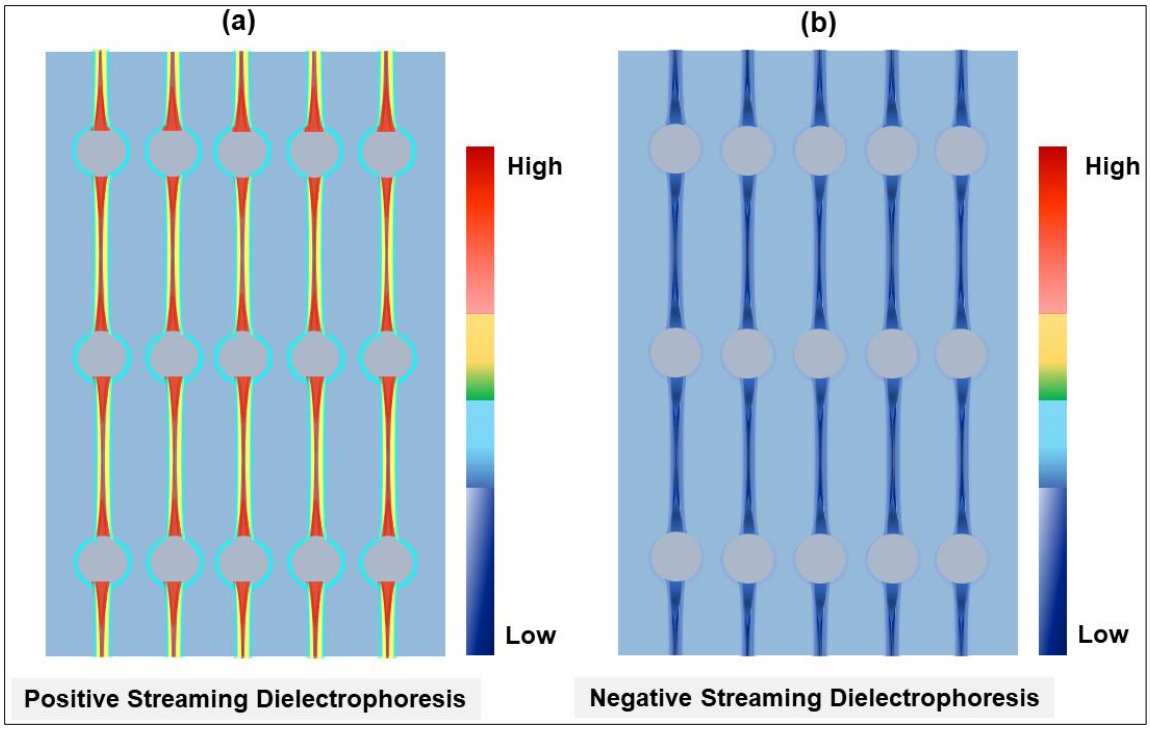

Figure 2.8: Schematic illustration of streaming DEP in a non-uniform electric field distribution. (a) During positive streaming DEP, the maximum concentration typically forms along the posts, and (b) during negative streaming DEP, the maximum concentration typically diminishes along the posts.

There are two categories of streaming DEP: positive streaming DEP and negative streaming DEP. When positive streaming DEP occurs, the maximum concentration is formed along the posts[37, 38, 6] as depicted in Figure 2.8(a). In case of positive streaming DEP, particles tend to gather along the centerline of the posts, resulting in a phenomenon termed enhancement[38]. Additionally, when negative streaming DEP occurs, the maximum concentration is depleted along the posts[37, 38, 6] as depicted in Figure 2.8(b). For negative streaming DEP case, particles tend to repel along the centerline of the posts, resulting in a phenomenon termed depletion[38]. Furthermore, several numerical and experimental study

showed that streaming DEP dependent on several parameters which are pH, electroosmotic mobility, electrophoretic mobility, DEP mobility as well as surfactant interaction.[37, 38, 6]

2.2.5 Protein Dielectrophoresis

The manipulation of proteins using an external electric field is of noteworthy interest for both fundamental studies of proteins and real-world applications. Nevertheless, an extensive understanding of the mechanisms underlying this process is yet required, and a robust theoretical model has still to be established[8].

Hölzel and Pethig have recently explored the limitations of the existing "classical" DEP theory for elucidating the experimental manipulation of proteins[10,14]. Some studies in protein DEP including the initial report emphasized that most experiments have been conducted by utilizing electric field gradients significantly lower than the minimum value predicted by the standard DEP theory[8,10,14]. The reason behind this unexpected discrepancy is that proteins possess net positive or negative charges which contribute to their permanent dipole moment. As a result, in a DEP experiment, the total dipole moment of a protein should encompass both permanent and induced dipole moments. However, the classical DEP theory only addresses the induced dipole moment. Consequently, the actual polarizability of proteins may increase by several orders of magnitude compared to what is predicted by conventional macroscopic theory and the required electric field gradient needed for DEP is significantly diminished[8,10,14].

Recently, Colburn and Matyushov[12] provided a model for estimating the DEP force acting on proteins which is referred to as CM polarization mechanism. According to the model the DEP force equation is:

$$\boldsymbol{F}_{DEP} = \varepsilon_0 \chi_{\mathrm{DEP}} \boldsymbol{\nabla E}^2 \quad (2.2.5.1)$$

where, ε_0 is the vacuum permittivity, χ_{DEP} is the DEP susceptibility. The ε_0 value is known and the value of the $\boldsymbol{\nabla E}^2$ can be estimated but determining and measuring χ_{DEP} is the primary challenge in advancing the theoretical comprehension of DEP. χ_{DEP} is related to the polarization parameter K[12],

$$\chi_{\mathrm{DEP}} = \frac{3}{2} \varepsilon_s \Omega_0 K \qquad (2.2.5.2)$$

Here, $\Omega_0 = (\frac{4\pi}{3}) r_0^3$, $K = K_{CM}$ and $K_{CM} = \frac{(\varepsilon_p - \varepsilon_m)}{(\varepsilon_p + 2\varepsilon_m)} \simeq -\frac{1}{2}$

According to the CM polarization mechanism, $\chi_{\mathrm{DEP}}^{\mathrm{CM}}$ (the DEP susceptibility derived from the CM polarization mechanism) is proportional to the radius of the proteins[12]:

$$\chi_{\mathrm{DEP}}^{\mathrm{CM}} = \frac{3}{2} \varepsilon_s \Omega_0 r_0^3 \qquad (2.2.5.3)$$

Proteins encompass both permanent and induced dipole moments and an alternative mechanism of inducing a dipole at the particle is recently proposed by Colburn and Matyushov[12] where the χ_{DEP}^{d} (the DEP susceptibility derived from the dipolar mechanism) is proportional to the dipole moment of the proteins[12].

$$\chi_{\mathrm{DEP}}^{\mathrm{d}} = \frac{\varepsilon_s^2}{6\varepsilon_0} \beta \chi_c M_0^2 \qquad (2.2.5.4)$$

Interestingly, recent reviews have addressed the inquiry regarding the minimal $\boldsymbol{\nabla E}^2$ necessary for protein trapping[10,14,12,16,17]. Typically estimated $\boldsymbol{\nabla E}^2$ required according to the CM polarization mechanism are on the order of 10^{21} V^2/m^3.[10,14,12,16,17] However, several researchers[8,10,14,12,16,17] demonstrated the capture of proteins at a much lower $\boldsymbol{\nabla E}^2$ sometimes down to 10^{12} V^2/m^3.[7,17] Recently, Colburn and Matyushov[12] provided a dipolar

mechanism for proteins and according to the dipolar mechanism, the estimated $\boldsymbol{\nabla E^2}$ required for capturing proteins is on the order of 10^{17} V^2/m^3.[12]

CHAPTER 3

NUMERICAL MODELING FOR IMPROVED ELECTRIC FIELDS AND GRADIENTS THEREOF

To explore the dielectrophoretic characteristics of nanometer-sized proteins, extremely high electric fields and gradients thereof are required to be generated in the microfluidic devices[17]. According to the theoretical study conducted by Matyushov et. al[12,15], the estimated $\boldsymbol{\nabla E^2}$ required is on the order of 10^{21} V^2/m^3 as stated by the CM polarization mechanism[10,14,12,16,17] which considered the Clausius-Mossotti factor of proteins to overcome the electrokinetic forces and to make the DEP force the most dominant force[10]. However, according to the literature, various researchers[10,14,12,16,17] reported protein capture occurring at significantly lower $\boldsymbol{\nabla E^2}$. Researchers successfully demonstrated the trapping of various proteins of sizes ranging from 6 kDa to 900 kDa using an electrode-based dielectrophoresis technique, and the required $\boldsymbol{\nabla E^2}$ as estimated by the researchers ranged from 10^{13} V^2/m^3 to 10^{24} V^2/m^3.[17] Moreover, researchers successfully demonstrated trapping of various proteins of sizes ranging from 1.5 kDa to 520 kDa using an insulator based dielectrophoresis technique and the required $\boldsymbol{\nabla E^2}$ was estimated to be in a range from 10^{12} V^2/m^3 to 10^{23} V^2/m^3.[17] Most recently, Matyushov et. al.[12] provided a new theoretical model, based on a dipolar mechanism which considered the dipole moment of proteins where the estimated $\boldsymbol{\nabla E^2}$ required for capturing proteins is on the order of 10^{17} V^2/m^3.[12]

To investigate strategies to get higher $\boldsymbol{\nabla E^2}$ for exploring the dielectrophoretic characteristics of the nm-sized proteins and to predict the trapping regions for the pDEP and nDEP cases, numerical modeling was performed with COMSOL Multiphysics 6.0.

3.1 Numerical Modeling

At first, in COMSOL Multiphysics 6.0, a section of the microfluidic device was drawn which contains a circular post array as depicted in Figure 3.1. The medium which is used for performing the simulation is water. The conductivity of the medium (σ) was adjusted to 0.03 S/m and a relative permittivity (ε_w) of 80 was used.

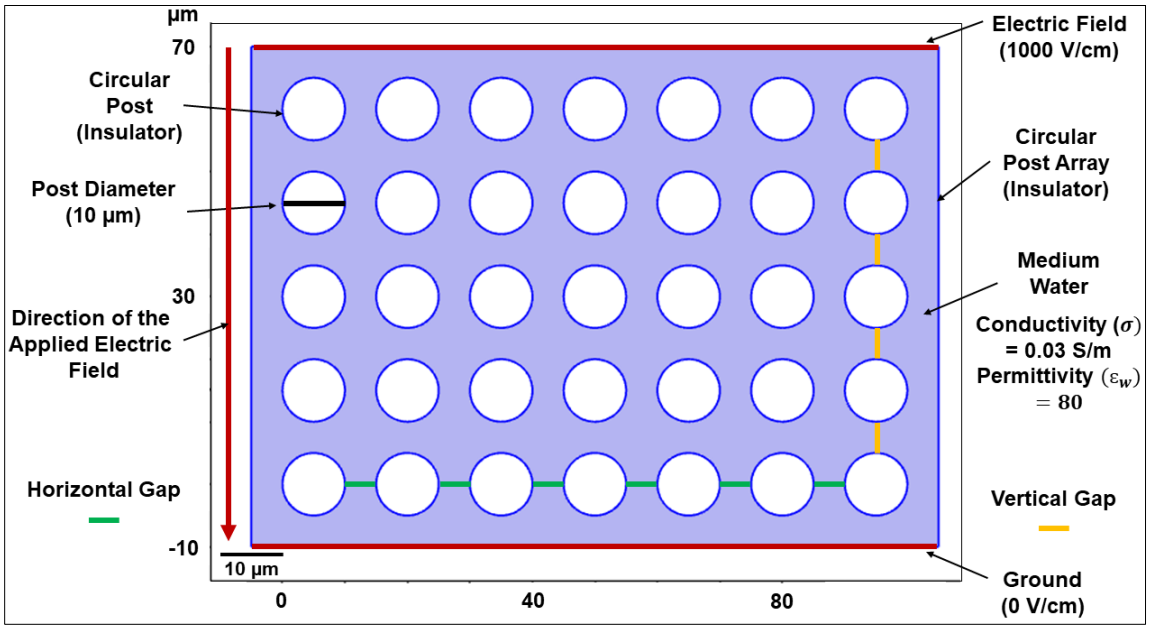

Figure 3.1: Illustration of the arrangement of the COMSOL simulation setup demonstrating some parameters utilized for conducting the simulation.

The module that was applied to compute the electric field distribution within the section was the electric current module. Maxwell's equation was applied to study the distribution of the electric field under static conditions, with the following equations:

$$\nabla \cdot \mathbf{J} = Q_{j,v} \quad (1)$$

$$\mathbf{J} = \sigma \mathbf{E} + \mathbf{J}_e \quad (2)$$

$$\mathbf{E} = -\nabla V \quad (3)$$

where $\nabla \cdot \mathbf{J}$ is the divergence of the current density, $Q_{j,v}$ is the volumetric source of current, $\mathbf{J}$ is the current density, σ is the medium conductivity, $\mathbf{E}$ is the electric field, $\mathbf{J_e}$ is the external current density, and V is the potential. A potential was applied matching the electric field in the experiment scaled to the channel section at the extremities of the channel section. The potential was applied to the inlet boundary, and the outlet was grounded as depicted in Figure 3.1. An extremely fine mesh was used for the computation.

3.2 Results

To investigate strategies to get higher $\nabla \boldsymbol{E}^2$ for exploring the dielectrophoretic characteristics of the nm-sized proteins, two types of numerical modeling studies were performed with COMSOL Multiphysics 6.0. In one study the gap between the posts was varied to observe the change in the $\nabla \boldsymbol{E}^2$. Furthermore, in another study, both the channel constriction and the gap in between the posts were varied to observe the change in the $\nabla \boldsymbol{E}^2$.

3.2.1. Variation of the Post-to-Post Gap

The variation of the magnitude of the electric field was explored by varying the post-to-post gap from 10 µm down to 100 nm. In Figure 3.2(a), 3.2(b), and 3.2(c), the numerically calculated $\nabla \boldsymbol{E}^2$ in the circular post array in a representative portion of the microfluidic device was represented. Figure 3.2(a) represented the distribution of $\nabla \boldsymbol{E}^2$ in a post array with a vertical post-to-post gap of 5 µm, a horizontal post-to-post gap of 10 µm and for an applied electric field of 1000 V/cm. The maximum value of the $\nabla \boldsymbol{E}^2$ resulted in 1.01 x 10^{16} V^2/m^3. As illustrated in Figure 3.2(b), when the vertical post-to-post gap remained at 5 µm but the horizontal post-to-post gap decreased from 10 µm to 5 µm and

for an applied electric field of 1000 V/cm, the value of the $\boldsymbol{\nabla E^2}$ increased to 1.10 x 10^{16} V^2/m^3. As demonstrated in Figure 3.2(c), when the vertical post-to-post gap remained 5 µm but the horizontal post-to-post gap decreased from 5 µm to 500 nm and for an applied electric field of 1000 V/cm, the value of the $\boldsymbol{\nabla E^2}$ increased to 2.49 x 10^{16} V^2/m^3.

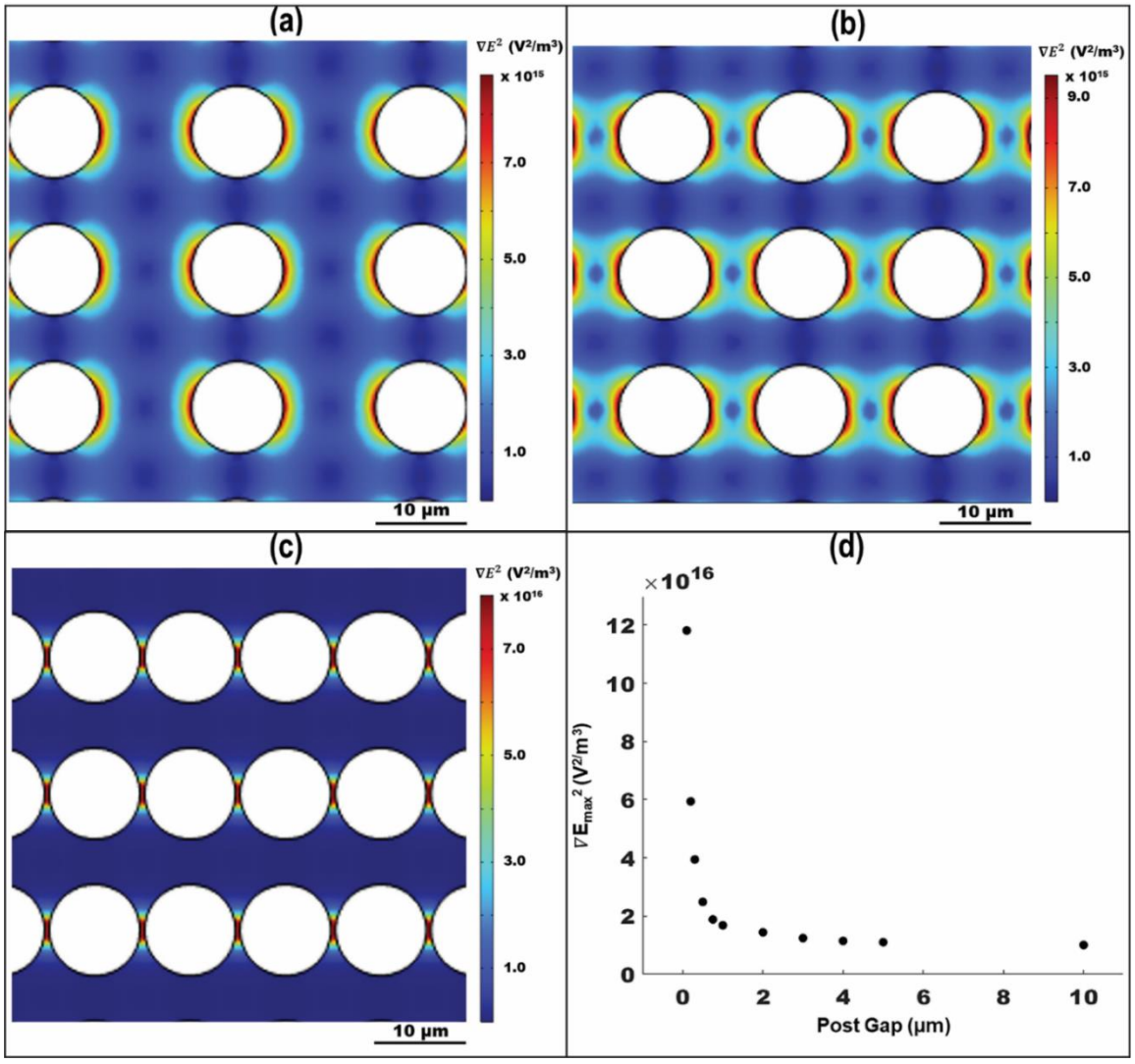

Figure 3.2: Variation in $\boldsymbol{\nabla E^2}$ with different post-to-post gaps for an applied electric field of 1000 V/cm. The horizontal post-to-post gap was varied, and the vertical post-to-post gap was 5 µm. (a) The horizontal gap between the two circular posts was 10 µm resulting in $\boldsymbol{\nabla E^2}$ of 1.01 x 10^{16} V^2/m^3, (b) The horizontal gap between the two circular posts was reduced to 5 µm resulting in $\boldsymbol{\nabla E^2}$ of 1.10 x 10^{16} V^2/m^3, (c) The horizontal gap between

the two circular posts was 500 nm, resulting in $\boldsymbol{\nabla E^2}$ of 2.49 x 10^{16} V^2/m^3, and (d) Maximum $\boldsymbol{\nabla E^2}$ values were predicted for various horizontal post-to-post gaps ranging from 10 μm to 100 nm resulting in a ~12 fold increase in $\boldsymbol{\nabla E^2}$ for the smallest post-to-post gap.

In Figure 3.2(d), the estimated $\boldsymbol{\nabla E^2}$ obtained from the numerical simulation study for post-to-post gaps from 10 μm to 100 nm were plotted. For the smallest post-to-post gap, the value of $\boldsymbol{\nabla E^2}$ increased by ~12 fold. Figure 3.2(d) confirmed the increment of $\boldsymbol{\nabla E^2}$ when the gap between the posts was decreased. The numerical simulation results provided an attainable strategy to generate higher $\boldsymbol{\nabla E^2}$ values by decreasing the post-to-post gap distance in the array of the iDEP microfluidic device for exploring the dielectrophoretic characteristics of nm-sized proteins.

3.2.2. Variation of the Channel Constriction and Post-to-Post Gap

The variation of the magnitude of the electric field was explored by varying both the channel constriction and the post-to-post gap. For performing the numerical modeling simulation, six different microfluidic designs with different constrictions and different post-to-post gaps were used as demonstrated in Figure 3.3. The length for all microfluidic devices was 2312 μm. The applied electric field for performing the numerical modeling simulations was 1000 V/cm. In Table 3.1, the maximum estimated $\boldsymbol{\nabla E^2}$ values in the pDEP trapping position ($\boldsymbol{\nabla E^2_{trap\_max}}$) and the minimum estimated $\boldsymbol{\nabla E^2}$ values in the pDEP trapping position ($\boldsymbol{\nabla E^2_{trap\_min}}$) were tabulated from the numerical modeling simulations for all six designs.

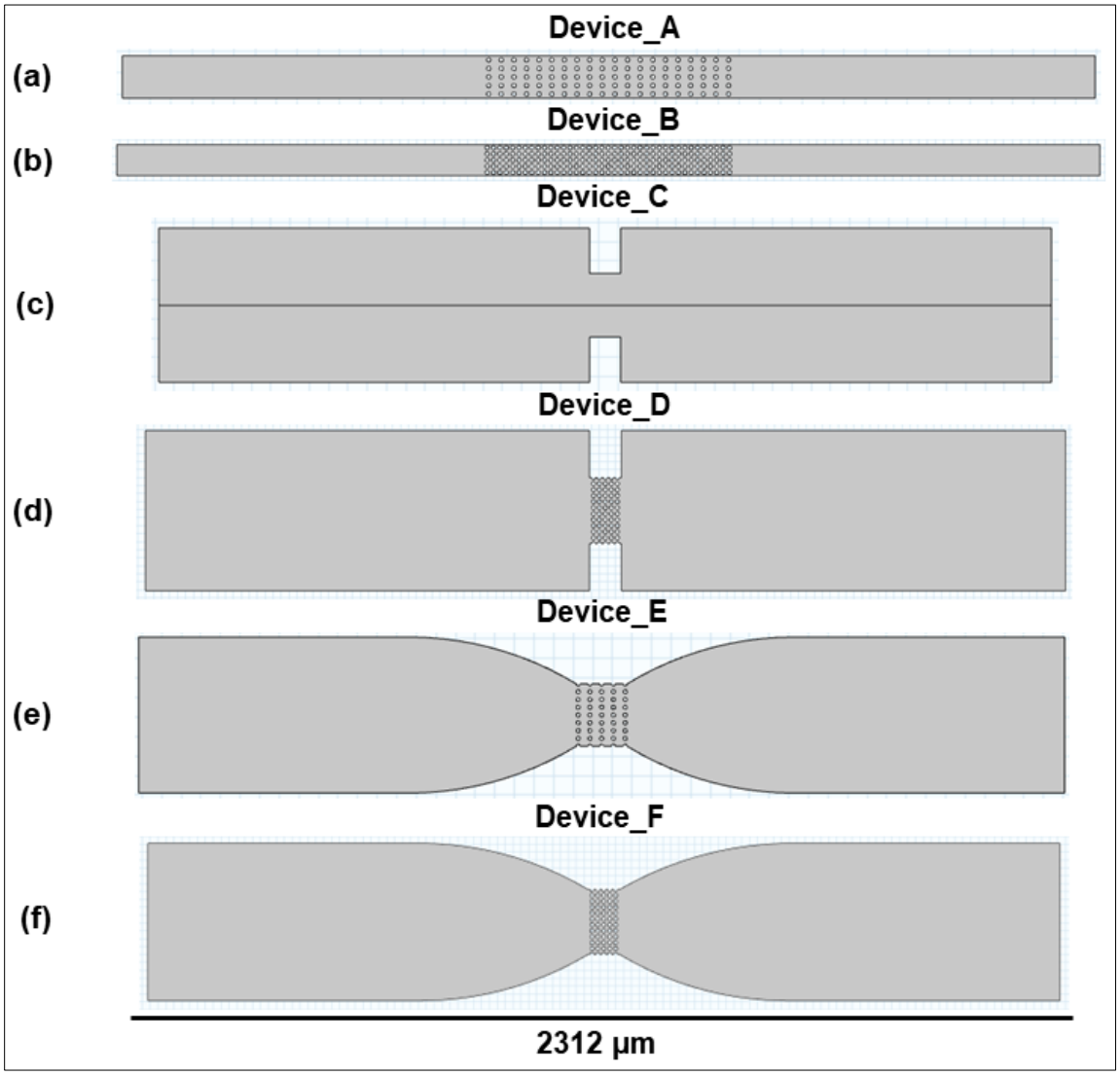

Figure 3.3: Six different designs of microfluidic devices with different constrictions and different post-to-post gaps explored with the numerical simulation. (a) Straight channel device with horizontal post-to-post gap of 20 µm and vertical post-to-post gap of 10 µm, (b) Straight channel device with both horizontal and vertical post-to-post gap of 5 µm, (c) Rectangular channel device without any posts, (d) Rectangular channel device with both horizontal and vertical post-to-post gap of 5 µm, (e) Curved channel device with horizontal post-to-post gap of 20 µm and vertical post-to-post gap of 10 µm, (f) Curved channel device with both horizontal and vertical post-to-post gap of 5 µm.

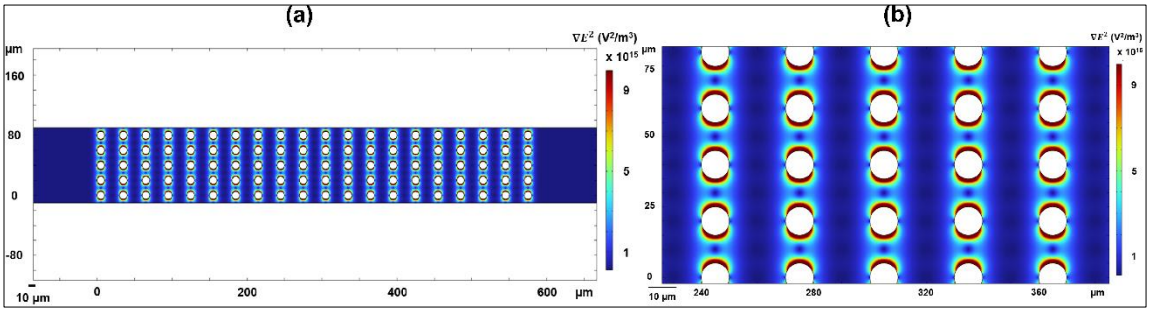

Figure 3.4: Computed distribution of ∇E^2 in a straight channel device having a circular post array, with horizontal post-to-post gap of 20 μm and vertical post-to-post gap of 10 μm (Device_A). The applied electric field was 1000 V/cm. (a) A segment of the microfluidic channel and circular post array, and (b) An enlarged segment of the circular post array.

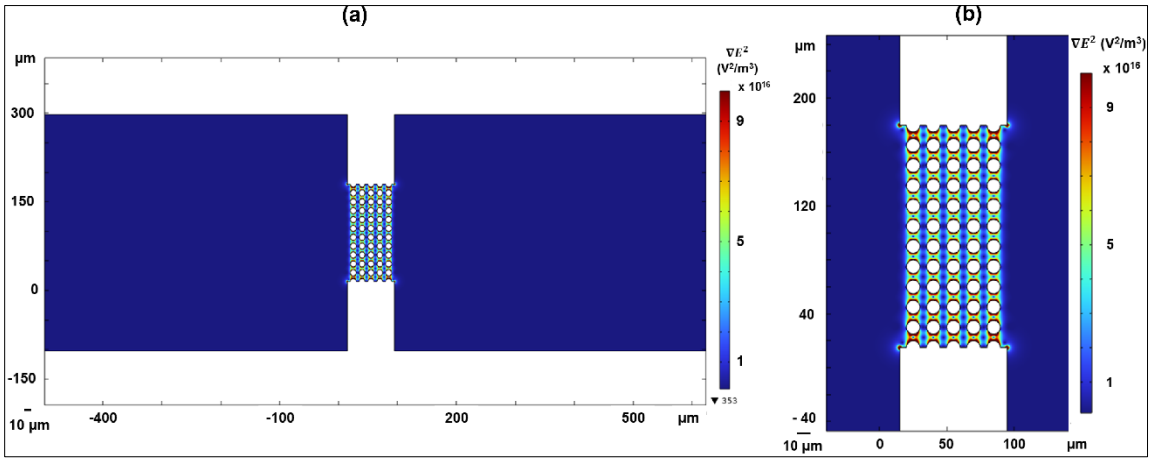

Figure 3.5: Computed distribution of ∇E^2 in a rectangular constriction device having a circular post array, with horizontal and vertical post-to-post gap of 5 μm (Device_D). The applied electric field was 1000 V/cm. (a) A section of the microfluidic channel and circular post array, and (b) A magnified section of the microfluidic channel and circular post array.

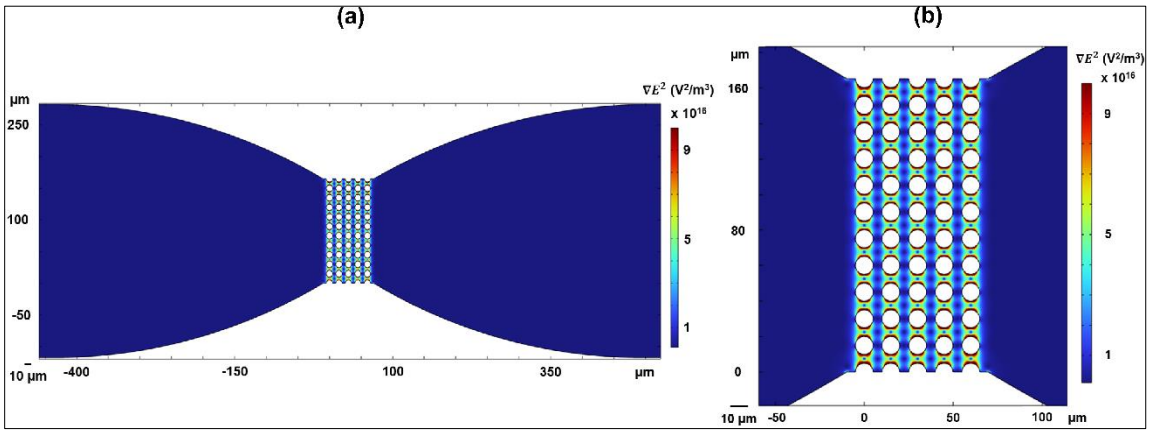

Figure 3.6: Computed distribution of $\boldsymbol{\nabla E^2}$ in a curved constriction device having a circular post array, with horizontal and vertical post-to-post gap of 5 μm (Device_F). The applied electric field was 1000 V/cm. (a) A section of the microfluidic channel and circular post array, and (b) A magnified section of the microfluidic channel and circular post array.

Table 3.1: Magnitude of the maximum estimated $\boldsymbol{\nabla E^2}$ values in the pDEP trapping position ($\boldsymbol{\nabla E^2_{trap\_max}}$) and the minimum estimated $\boldsymbol{\nabla E^2}$ values in the pDEP trapping position ($\boldsymbol{\nabla E^2_{trap\_min}}$) of all the six designs of microfluidic devices

Device	$\boldsymbol{\nabla E^2_{trap\_max}}$	$\boldsymbol{\nabla E^2_{trap\_min}}$
Device_A	2.28 x 10^{16}	2.28 x 10^{16}
Device_B	2.99 x 10^{16}	2.98 x 10^{16}
Device_C	2.44 x 10^{14}	5.62 x 10^{10}
Device_D	2.79 x 10^{17}	1.67 x 10^{17}
Device_E	1.32 x 10^{17}	8.80 x 10^{16}
Device_F	2.12 x 10^{17}	1.61 x 10^{17}

3.2.2.1 Comparison Between the Devices Having Similar Channel Constriction but Different Post-to-Post Gap

As demonstrated in Figures 3.3(A) and 3.2(B), Device_A and Device_B featured a straight channel. For Device_A, the horizontal post-to-post gap was 20 μm, the vertical post-to-post gap was 10 μm and the generated maximum $\boldsymbol{\nabla E^2}$ was 2.28 x 10^{16} V^2/m^3 [Figures 3.3(A) and 3.4, and Table 3.1]. For Device_B, the horizontal post-to-post gap was 5 μm which was ~4 times lower and the vertical post-to-post gap was 5 μm which was ~2 times lower in comparison to Device_A and the generated maximum $\boldsymbol{\nabla E^2}$ was 2.99 x 10^{16} V^2/m^3 [Figure 3.3(B) and Table 3.1]. The result showed ~1.3 times increment in the $\boldsymbol{\nabla E^2}$ from Device_A to Device_B.

As demonstrated in Figures 3.3(C) and 3.3(D), Device_C and Device_D had a rectangular channel constriction. Device_C did not contain any posts inside the microfluidic channel and the generated maximum $\boldsymbol{\nabla E^2}$ was 2.44 x 10^{14} V^2/m^3 [Figure 3.3(C) and Table 3.1]. For Device_D, both the horizontal and vertical post-to-post gap were 5 μm and the generated maximum $\boldsymbol{\nabla E^2}$ was 2.79 x 10^{17} V^2/m^3 [Figures 3.3(D) and 3.5, and Table 3.1]. The result showed a ~3 order of magnitude increment in the $\boldsymbol{\nabla E^2}$ from Device_C to Device_D.

As demonstrated in Figures 3.3(E) and 3.3(F), the microfluidic devices, Device_E and Device_F, had a curved channel constriction. However, for Device_E, the horizontal post-to-post gap was 20 μm, the vertical post-to-post gap was 10 μm and the maximum $\boldsymbol{\nabla E^2}$ was 1.32 x 10^{17} V^2/m^3 [Figure 3.3(E) and Table 3.1]. For Device_F, the horizontal post-to-post gap was 5 μm which was ~4 times lower and the vertical post-to-post gap was 5 μm which was ~2 times lower in comparison to Device_E and the generated maximum

∇E^2 was 2.12 x 10^{17} V^2/m^3 [Figures 3.3(F), 3.6 and Table 3.1]. The result showed ~1.6 times increment in the ∇E^2 from Device_E to Device_F.

From the above discussion, it can be concluded that if the horizontal and vertical post-to-post gap were varied in the microfluidic device, but channel constrictions of the microfluidic device remained similar then it is feasible to increase the ∇E^2 in the microfluidic device.

3.2.2.2 Comparison Between the Devices Having Different Channel Constriction but Similar Post-to-Post Gap

When comparing Device_B, Device_D, and Device_F, all three devices had the same horizontal and vertical post-to-post gap of 5 µm, however, the channel constriction was different among the three devices.

For Device_B with a straight channel, the maximum ∇E^2 was 2.99 x 10^{16} V^2/m^3 [Figure 3.2(B) and Table 3.1]. For Device_D with rectangular channel constriction, the maximum ∇E^2 was 2.79 x 10^{17} V^2/m^3 [Figures 3.2(D) and 3.5, and Table 3.1] and the ∇E^2 was ~9.3 times higher in comparison to Device_B. Interestingly, by adding a rectangular channel constriction, the ∇E^2 was increased by ~9.3 times. For Device_F with curved channel constriction, the maximum ∇E^2 was 2.12 x 10^{17} V^2/m^3 [Figures 3.2(F) and 3.6, and Table 3.1] and the ∇E^2 was ~7.1 times higher in comparison to Device_B. Interestingly, by adding a curved channel constriction, the ∇E^2 was increased by ~7.1 times. Moreover, the results demonstrated that in Device_D by adding a rectangular channel constriction, the ∇E^2 was increased by ~1.3 times in comparison to the ∇E^2 of Device_F where a curved constriction was added.

Furthermore, comparing Device_A and Device_E with the same horizontal post-to-post gap of 20 µm and the same vertical post-to-post gap of 10 µm, the channel constriction was varied between the two devices. For Device_A, with straight channel, the maximum $\boldsymbol{\nabla E^2}$ was 2.28 x 10^{16} V^2/m^3 [Figures 3.2(A) and 3.4, and Table 3.1]. For, Device_E with curved channel constriction, the maximum $\boldsymbol{\nabla E^2}$ was 1.32 x 10^{17} V^2/m^3 [Figure 3.2(E) and Table 3.1] and the $\boldsymbol{\nabla E^2}$ was ~5.8 times higher in comparison to Device_A. By adding a curved channel constriction, the $\boldsymbol{\nabla E^2}$ was increased by ~5.8 times.

It can be concluded that if the horizontal and vertical post-to-post gap was similar, but the channel constriction changed from rectangular to curved, the value of the $\boldsymbol{\nabla E^2}$ can be increased.

From the results of the numerical modeling simulation as discussed in Section 3.2.2 and as demonstrated in Table 3.1, Device_A [Figure 3.2(A)] generated the lowest maximum $\boldsymbol{\nabla E^2}$ which was 2.28 x 10^{16} V^2/m^3 and Device_B [Figure 3.2(B)] generated the second lowest maximum $\boldsymbol{\nabla E^2}$ which was 2.99 x 10^{16} V^2/m^3 among all the five devices containing posts inside the microfluidic channel. Furthermore, Device_D [Figure 3.2(D)] generated the highest maximum $\boldsymbol{\nabla E^2}$ which was 2.79 x 10^{17} V^2/m^3, Device_F [Figure 3.2(F)] generated the second highest maximum $\boldsymbol{\nabla E^2}$ which was 2.12 x 10^{17} V^2/m^3 and Device_E [Figure 3.2(E)] generated the third highest maximum $\boldsymbol{\nabla E^2}$ which was 1.32 x 10^{17} V^2/m^3.

3.2.3. Influence of Post Location on ∇E^2

In Section 3.2.2, the magnitude of the maximum $\boldsymbol{\nabla E^2}$ and the variation of the maximum $\boldsymbol{\nabla E^2}$ of all six microfluidic devices were discussed. However, from the

discussion in Section 3.2.2, the variation of $\boldsymbol{\nabla E^2}$ within the post array was not discussed. To explore this, further analysis was performed using numerical modeling simulations.

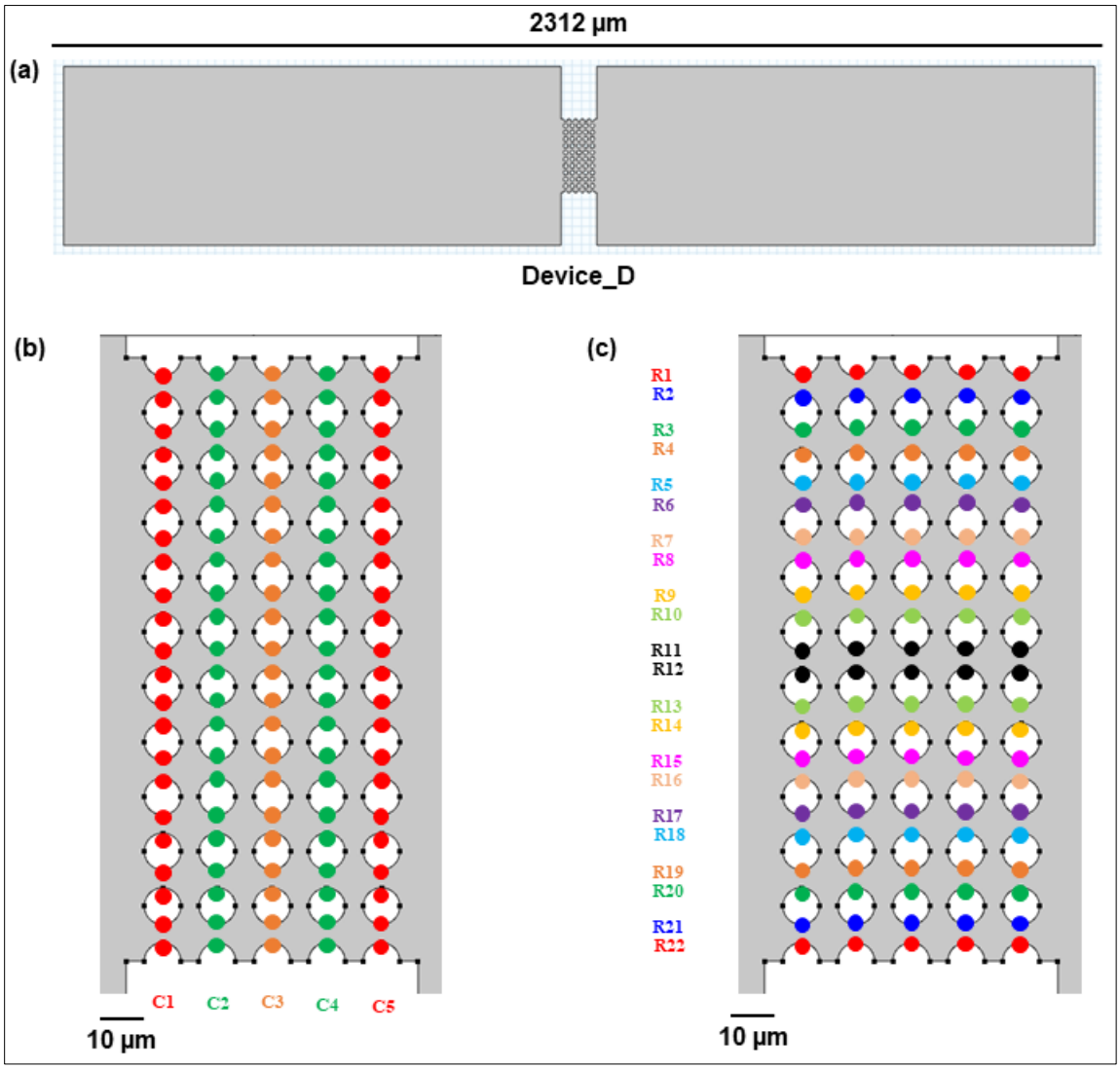

Figure 3.7: (a) Rectangular channel device with horizontal and vertical post-to-post gap of 5 µm (Device_D), (b) Five post columns used to estimate the maximum $\boldsymbol{\nabla E^2}$ (Device_D) and (c) Twenty-two post rows used to estimate the maximum $\boldsymbol{\nabla E^2}$ (Device_D). The color scheme denotes the columns and rows with similar characteristics.

To estimate the maximum $\boldsymbol{\nabla E^2}$ along columns and rows, a point evaluation method was used in the numerical model. One example was demonstrated in Figure 3.7(a) of

Device_D. As shown in Figure 3.7(b), there were five columns with posts and the maximum $\boldsymbol{\nabla E^2}$ of all points along the columns were tabulated. Moreover, as shown in Figure 3.7(c), there were twenty-two rows with posts and the maximum $\boldsymbol{\nabla E^2}$ of all points along the rows were tabulated.

As shown in Figure 3.8, for Device_A, the maximum $\boldsymbol{\nabla E^2}$ along the column 1 (C1) to column 20 (C20) and along the row 1 (R1) to row 10 (R10) was similar which was 2.28 x 10^{16} V^2/m^3. It can thus be concluded that the maximum $\boldsymbol{\nabla E^2}$ was uniform through the columns and rows of Device_A.

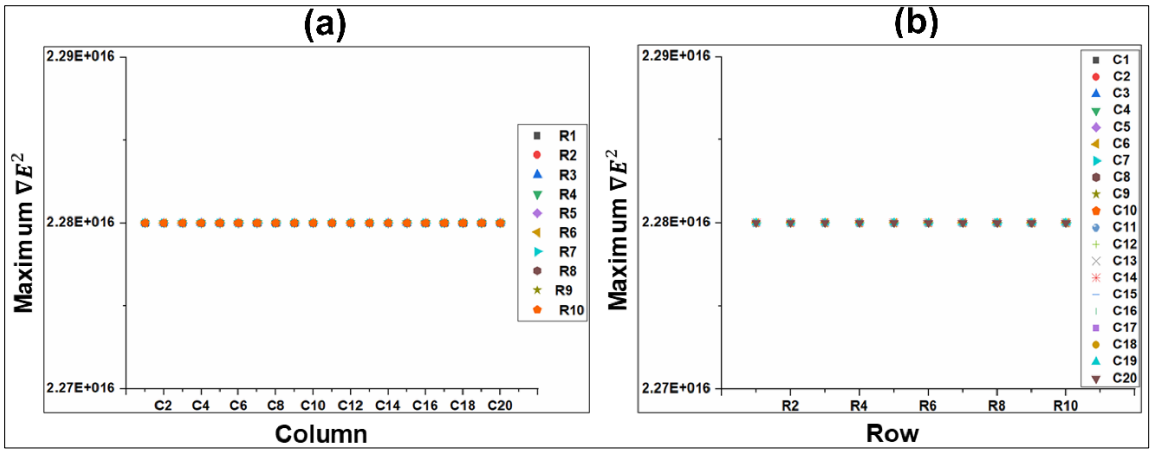

Figure 3.8: Variation of the maximum $\boldsymbol{\nabla E^2}$ with respect to the (a) column and (b) row for Device_A.

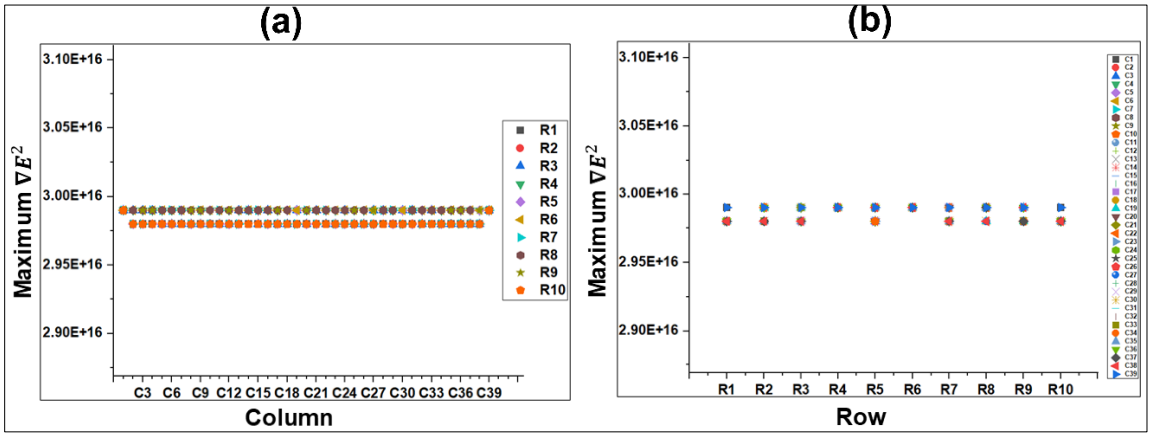

Figure 3.9: Variation of the maximum $\boldsymbol{\nabla E^2}$ with respect to the (a) column and (b) row for Device_B.

As shown in Figure 3.9 (a) and (b), for Device_B, the maximum $\boldsymbol{\nabla E^2}$ along the column 1 (C1) to column 39 (C39) and along the row 1 (R1) to row 10 (R10) were nearly identical. Specifically, two $\boldsymbol{\nabla E^2}$ values were observed; 2.99 x 10^{16} V^2/m^3 and 2.98 x 10^{16} V^2/m^3, with a mere difference of 0.01 x 10^{16} V^2/m^3 in $\boldsymbol{\nabla E^2}$. Therefore, it can be inferred that the maximum $\boldsymbol{\nabla E^2}$ was nearly uniform across the columns and rows of Device_B.

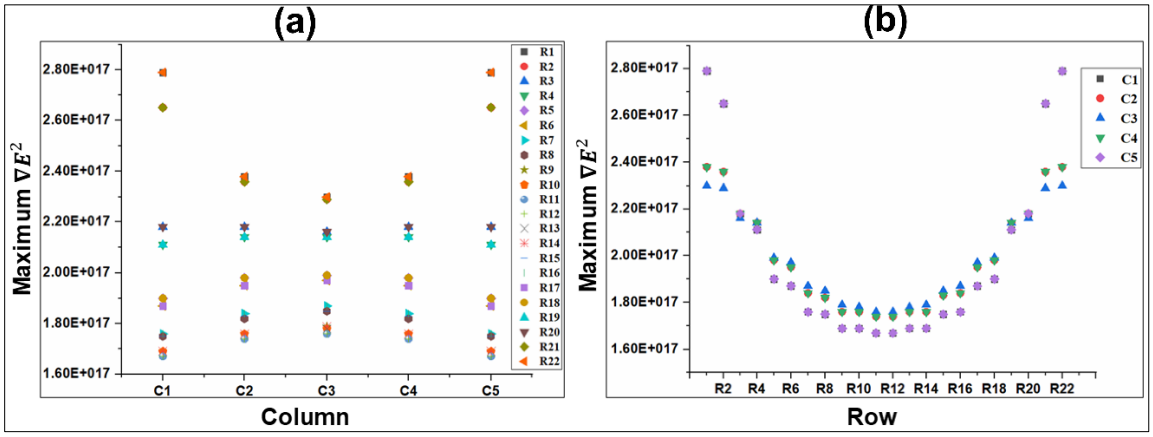

Figure 3.10: Variation of the maximum $\boldsymbol{\nabla E^2}$ with respect to the (a) column and (b) row for Device_D.

As demonstrated in Figure 3.10(a) for Device_D, the maximum $\boldsymbol{\nabla E^2}$ along the column 1 (C1) to column 5 (C5) was dissimilar. For column 1 (C1) and column 5 (C5), the highest maximum $\boldsymbol{\nabla E^2}$ was 2.79 x 10^{17} V^2/m^3. For column 2 (C2) and column 4 (C4), the highest maximum $\boldsymbol{\nabla E^2}$ was 2.38 x 10^{17} V^2/m^3, representing ~1.17 times lower $\boldsymbol{\nabla E^2}$ compared to the highest maximum $\boldsymbol{\nabla E^2}$ estimated in column 1 (C1) and column 5 (C5). For, column 3 (C3) the highest maximum $\boldsymbol{\nabla E^2}$ was 2.30 x 10^{17} V^2/m^3, representing ~1.21 times lower $\boldsymbol{\nabla E^2}$ compared to the highest maximum $\boldsymbol{\nabla E^2}$ estimated in column 1 (C1) and column 5 (C5). C1 and C5 generated the highest maximum $\boldsymbol{\nabla E^2}$, C2 and C4 generated the second highest maximum $\boldsymbol{\nabla E^2}$ and C3 generated the lowest highest maximum $\boldsymbol{\nabla E^2}$ among all columns.

Moreover, as demonstrated in Figure 3.10(b) for Device_D, through row 1 (R1) to row 22 (R22), the maximum $\boldsymbol{\nabla E^2}$ was different. For row 1 (R1) and row 22 (R22), the highest maximum $\boldsymbol{\nabla E^2}$ was 2.79 x 10^{17} V^2/m^3. For row 11 (R11) and row 12 (R12), the highest maximum $\boldsymbol{\nabla E^2}$ was 1.76 x 10^{17}, representing ~1.59 times lower $\boldsymbol{\nabla E^2}$ compared to the highest maximum $\boldsymbol{\nabla E^2}$ estimated in row 1 (R1) and row 22 (R22). The maximum $\boldsymbol{\nabla E^2}$ was highest at row 1 (R1) and then the maximum $\boldsymbol{\nabla E^2}$ started to decrease slowly. Row 11 (R11) and row 12 (R12) had the lowest maximum $\boldsymbol{\nabla E^2}$ and afterward, the maximum $\boldsymbol{\nabla E^2}$ increased slowly again and row 22 (R 22) generated again the highest maximum $\boldsymbol{\nabla E^2}$. So, it can be concluded that the maximum $\boldsymbol{\nabla E^2}$ was not uniform through the columns and rows of Device_D.

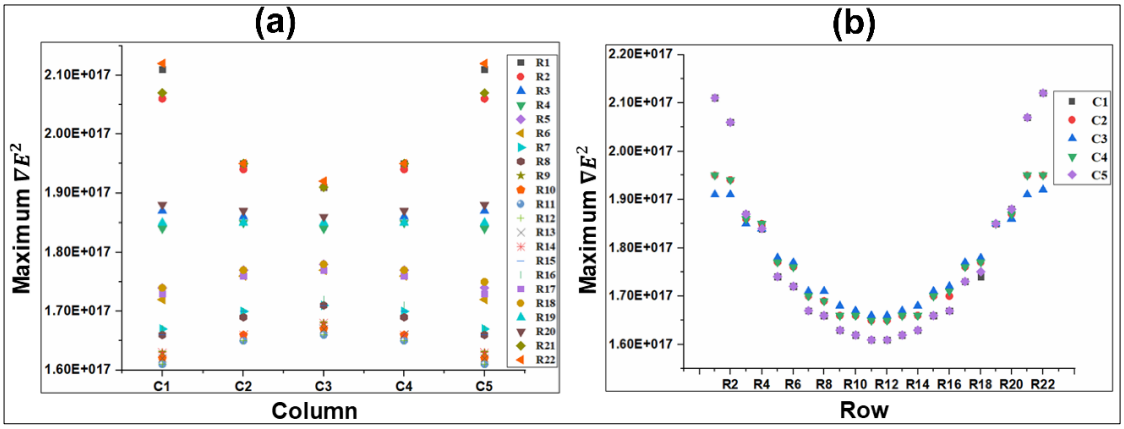

Figure 3.11: Variation of the maximum ∇E^2 with respect to the (a) column and (b) row for Device_F.

As demonstrated in Figure 3.11(a) for Device_F, the maximum ∇E^2 along the column 1 (C1) to column 5 (C5) was dissimilar. For column 1 (C1) and column 5 (C5), the highest maximum ∇E^2 was 2.12 x 10^{17} V^2/m^3. For column 2 (C2) and column 4 (C4), the highest maximum ∇E^2 was 1.95 x 10^{17} V^2/m^3, representing ~1.08 times lower ∇E^2 compared to the highest maximum ∇E^2 estimated in column 1 (C1) and column 5 (C5). For, column 3 (C3) the highest maximum ∇E^2 was 1.91 x 10^{17} V^2/m^3, representing ~1.11 times lower ∇E^2 compared to the highest maximum ∇E^2 estimated in column 1 (C1) and column 5 (C5). C1 and C5 generated the highest maximum ∇E^2, C2 and C4 generated the second highest maximum ∇E^2 and C3 generated the lowest maximum ∇E^2 among all columns. Moreover, as demonstrated in Figure 3.11(b) for Device_F, through row 1 (R1) to row 22 (R22), the maximum ∇E^2 was different. For row 1 (R1) and row 22 (R22), the highest maximum ∇E^2 was 2.11 x 10^{17} V^2/m^3. For row 11 (R11) and row 12 (R12), the highest maximum ∇E^2 was 1.66 x 10^{17}, representing ~1.27 times lower

$\boldsymbol{\nabla E^2}$ compared to the highest maximum $\boldsymbol{\nabla E^2}$ estimated in row 1 (R1) and row 22 (R22). The maximum $\boldsymbol{\nabla E^2}$ was highest at row 1 (R1) before gradually decreasing. Row 11 (R11) and row 12 (R12) had the lowest maximum $\boldsymbol{\nabla E^2}$, followed by a gradual increase until row 22 (R 22) once again generated the highest maximum $\boldsymbol{\nabla E^2}$. Therefore, it is evident that the maximum $\boldsymbol{\nabla E^2}$ was not uniform through the columns and rows of Device_F.

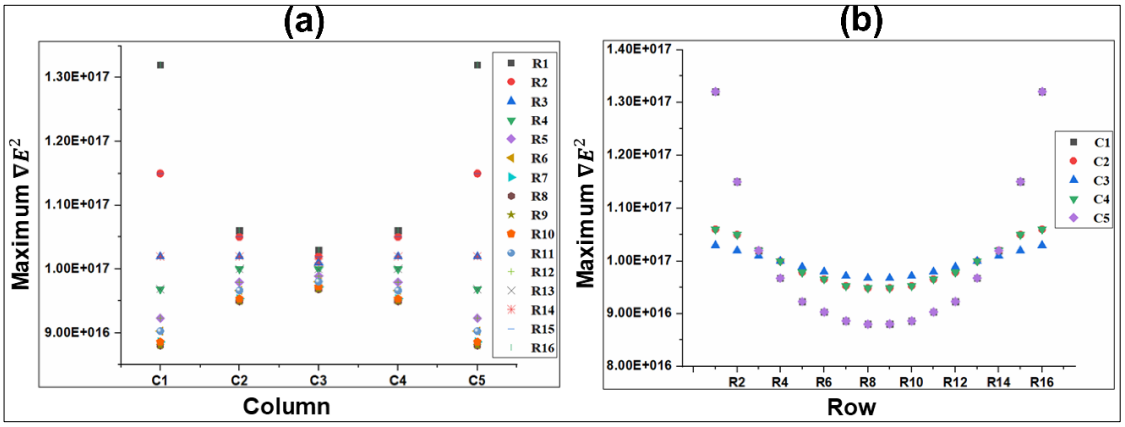

Figure 3.12: Variation of the maximum $\boldsymbol{\nabla E^2}$ with respect to the (a) column and (b) row for Device_E.

As shown in Figure 3.12(a) for Device_E, the maximum $\boldsymbol{\nabla E^2}$ along column 1 (C1) to column 5 (C) was different. For column 1 (C1) and column 5 (C5), the highest maximum $\boldsymbol{\nabla E^2}$ was 1.32 x 10^{17} V^2/m^3. For column 2 (C2) and column 4 (C4), the highest maximum $\boldsymbol{\nabla E^2}$ was 1.06 x 10^{17} V^2/m^3, representing ~1.25 times lower $\boldsymbol{\nabla E^2}$ compared to the highest maximum $\boldsymbol{\nabla E^2}$ estimated in column 1 (C1) and column 5 (C5). For, column 3 (C3) the highest maximum $\boldsymbol{\nabla E^2}$ was 1.03 x 10^{17} V^2/m^3, representing ~1.28 times lower $\boldsymbol{\nabla E^2}$ compared to the highest maximum $\boldsymbol{\nabla E^2}$ estimated in column 1 (C1) and column 5 (C5) in. C1 and C5 generated the highest maximum $\boldsymbol{\nabla E^2}$, while C2 and C4 resulted in the second highest maximum $\boldsymbol{\nabla E^2}$ and C3, on the other hand, yielded the lowest maximum $\boldsymbol{\nabla E^2}$

among all columns. Moreover, as demonstrated in Figure 3.12(b) for Device_E, through row 1 (R1) to row 16 (R16), the maximum $\boldsymbol{\nabla E^2}$ was different. For row 1 (R1) and row 16 (R16), the highest maximum $\boldsymbol{\nabla E^2}$ was 1.32 x 10^{17} V^2/m^3. For row 8 (R8) and row 9 (R9), the highest maximum $\boldsymbol{\nabla E^2}$ was 9.68 x 10^{16}, representing ~1.36 times lower $\boldsymbol{\nabla E^2}$ compared to the highest maximum $\boldsymbol{\nabla E^2}$ estimated in row 1 (R1) and row 16 (R16). The highest maximum $\boldsymbol{\nabla E^2}$ occurred at row 1 (R1) before progressively declining. Row 8 (R8) and row 9 (R9) exhibited the lowest maximum $\boldsymbol{\nabla E^2}$, followed by a gradual increase until row 16 (R16) once again generated the highest maximum $\boldsymbol{\nabla E^2}$. Therefore, it is evident that the distribution of maximum $\boldsymbol{\nabla E^2}$ was not uniform across the columns and rows of Device_F.

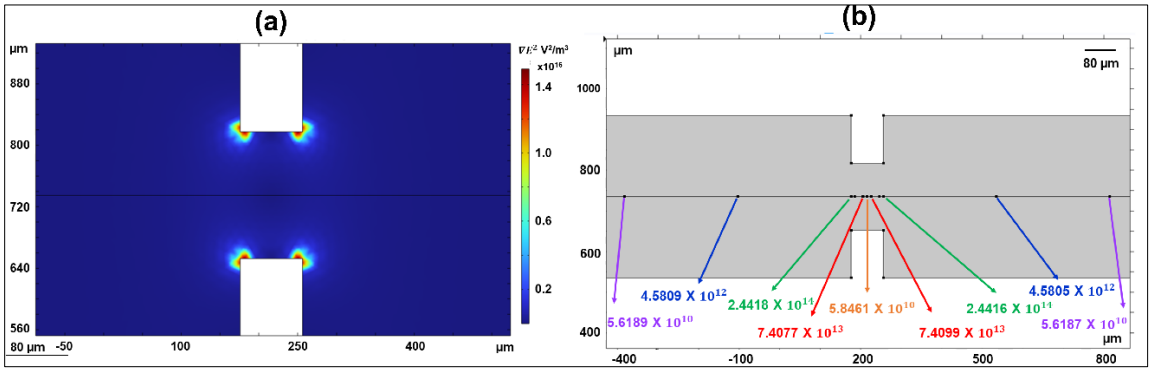

Figure 3.13: Variation in the $\boldsymbol{\nabla E^2}$ value within the wide and narrow channel of the microfluidic device. (a) Computed distribution of $\boldsymbol{\nabla E^2}$ in the wide and narrow channel of the microfluidic device at an applied electric field of 1000 V/cm, and (b) Estimated $\boldsymbol{\nabla E^2}$ value in the wide and narrow channel of the microfluidic device using the point evaluation method of the numerical model.

The variation in the $\boldsymbol{\nabla E^2}$ [Figure 3.13 (a)] and the estimated $\boldsymbol{\nabla E^2}$ within the wide and narrow channel of the microfluidic device of Device_C was demonstrated in Figure 3.13 (b). $\boldsymbol{\nabla E^2}$ was 5.62 x 10^{10} V^2/m^3 at the end of the wide channel and $\boldsymbol{\nabla E^2}$ was increased to 4.58 x 10^{12} V^2/m^3 near the constriction. At the edge of the rectangular constriction, $\boldsymbol{\nabla E^2}$

was highest at 2.44 x 10^{14} V^2/m^3. On the opposite side of the constriction, $\boldsymbol{\nabla E^2}$ started to decrease again and at the middle of the narrow channel, the $\boldsymbol{\nabla E^2}$ was lowest at 5.85 x 10^{10} V^2/m^3. Subsequently, the rate of increase in $\boldsymbol{\nabla E^2}$ resumed, reaching its highest once again at the edge of the rectangular constriction, where it showed the highest $\boldsymbol{\nabla E^2}$ of 2.44 x 10^{14} V^2/m^3. When the narrow channel ended and transitioned into the wide channel, the rate of change in $\boldsymbol{\nabla E^2}$ began to decline and at the opposite end of the wide channel, $\boldsymbol{\nabla E^2}$ reached a value of 5.62 x 10^{10} V^2/m^3. From Figure 3.13(a), it can be concluded that by adding the rectangular constriction, $\boldsymbol{\nabla E^2}$ can be increased and that $\boldsymbol{\nabla E^2}$ is highest at the edge of the rectangular constriction.

CHAPTER 4

TRANSLATING NUMERICAL MODELING INTO FABRICATING 3D-PRINTED MICROFLUIDIC DEVICES

In Chapter 3, it was interpreted that by decreasing the gap between the posts and by adding constrictions (e.g. rectangular or curved) in the microfluidic channel, the $\boldsymbol{\nabla E^2}$ can be increased in the microflucidic device. For translating the result of the numerical modeling into fabricating the microfluidic device, a two-photon polymerization-based (2PP) 3D printing technique was employed. 2PP 3D printing allows the fabrication of 3D prototypes directly from computer-aided-design (CAD) models.[29] There are some advantages of the 2PP 3D printing over the conventional photolithography. Using the 2PP 3D printing technique, it is possible to achieve rapid prototyping of microfluidic devices, and this is a cleanroom-free fabrication technique. Moreover, the 2PP 3D printing enables high-resolution fabrication. Thus, the 2PP 3D printing technique was employed to print and fabricate the 3D printed microfluidic devices.

4.1 Method of Printing and Fabricating the 3D Printed Microfluidic Device

The device layout and channel structure of Device_D and Device_F were designed in Fusion 360 (AutoDesk, USA) software as depicted in Figure 4.1 (a) and (b). Both devices consisted of an array with circular posts. The total length of the device was 5 mm, the horizontal and vertical post-to-post gap distance was 5 μm, and the post diameter was 10 μm. The inner diameter of the reservoir was 450 μm with a height of 600 μm. The post array channel length was 2.6 mm with a height of 50 μm as depicted in Figure 4.1 (a) and (b).

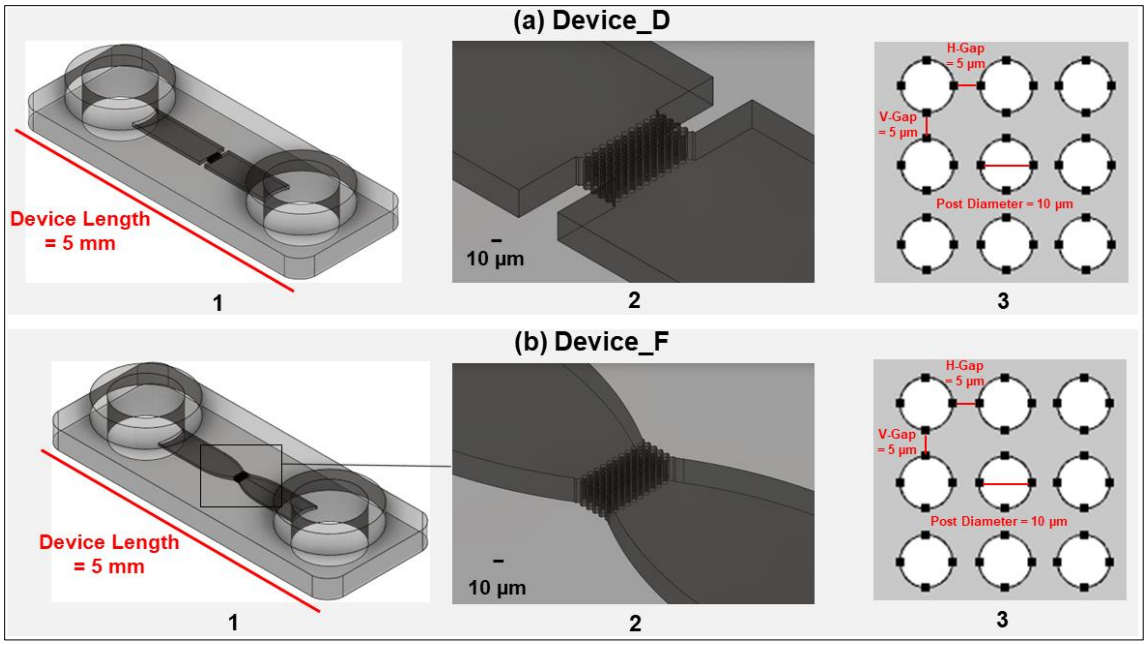

Figure 4.1: Fusion 360 design of the 3D printed microfluidic device. Panel (a) illustrated the Fusion 360 design of Device_D. Subpanels (a1) depicted the whole design of Device_D along with its dimensions, (a2) showcased a magnified section of the design of Device_D highlighting the circular posts, and (a3) provided a magnified section of the circular post array with detailed dimensions. Panel (b) illustrated the Fusion 360 design of Device_F. Subpanels (b1) presented the whole design of Device_F including its dimensions, (b2) displayed a magnified section of the design of Device_F featuring the circular posts, and (b3) provided a magnified section of the circular post array with specific dimensions.

The Fusion 360 file was converted into an STL file and imported into the DeScribe software of the Nanoscribe GT instrument. The printing parameters were adjusted in the Describe software. For printing both devices, a laser power of 80 and scan speed of 50000 was used. The Meso scale protocol was used to print 5 µm resolution in a Photonic Professional GT 3D-printer (Nanoscribe GmbH, Germany) with IP-S photoresist (Nanoscribe GmbH, Germany). At first, an indium tin oxide (ITO)-coated boroaluminosilicate glass slide was cleaned with isopropyl alcohol (IPA) and then dried with a stream of nitrogen gas. Afterward, the ITO glass slide was placed on the holder of

the Photonic Professional GT 3D-printer and the ITO glass was taped to the holder to secure it in that place. Then, a small drop of IP-S photoresist was deposited on top of the ITO glass and the holder containing the ITO glass slide was placed inside the printer. Afterward, the designed 3D structure was printed using the Photonic Professional GT 3D-printer (Nanoscribe GmbH, Germany). After printing, the device was developed. At first, the device was placed in a developing holder in a way where one reservoir was placed at the bottom and another reservoir was placed at the top. Then, the device and holder were placed in a beaker containing SU-8 developer. Afterward, the whole beaker was covered with foil and the beaker was placed in a shaker for about 3 hr. The beaker was then placed in a sonicator for 15 min. Subsequently, for additional refinement and complete removal of the photoresist from the device, the device underwent a thorough cleaning process with SU-8 developer under vacuum conditions. Approximately, a few mL SU-8 developer was introduced in each reservoir via vacuum flow, facilitating comprehensive cleaning of the device and removing excess photoresist residing between the posts. Then, the device was placed inside a beaker containing IPA, and the beaker was placed in the sonicator for 15 min for further development. Then, the developed device was dried and visually inspected with an optical microscope.

After proper development, the 3D printed device was assembled. A thin PDMS slab of 1.5 mm thickness was prepared and cut into small pieces. The thin PDMS slab was placed on top of a No.1 thickness glass slide of 0.17 mm thickness and glued together using epoxy glue. Finally, the developed 3D-printed device was placed on top of the thin PDMS slab and glued together using epoxy glue. Afterward, the assembled 3D printed device was kept in a petri dish.

4.2 Results of 3D-Printing of the Microfluidic Devices

First, Device_D was printed using the 2PP 3D printing technique. However, the printing and development process of the 3D printed microfluidic devices was not a straightforward and effortless process. Numerous difficulties and challenges were experienced during the printing and development process of the Device_D, e.g. the channels were not fully developed, and some non-developed photoresist was still present inside the channel after the development process. Furthermore, the posts were not fully developed, and the non-developed photoresist remained in between the posts. The fluorescence image and the brightfield image of Device_D were depicted in Figures 4.2(a) and 4.2(b)) indicate non-developed posts with non-developed photoresist remaining in between the posts.

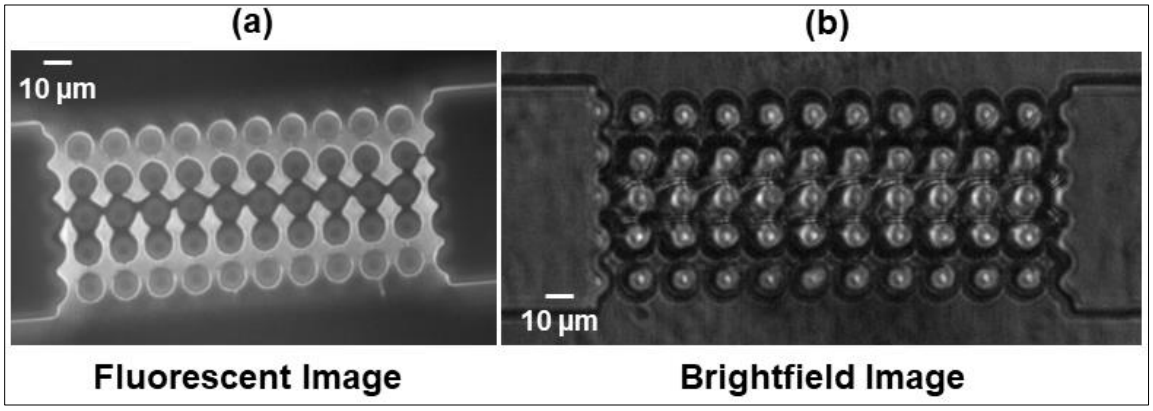

Figure 4.2: (a) Fluorescent image and (b) brightfield image of Device_D after development. A not fully developed post array was observed and photoresist in between the posts was detected.

To obtain a fully developed 3D printed microfluidic device, several changes were made to the printing parameters and the development procedure. During the printing of the 3D printed microfluidic device, a block printing method was used where the 3D printed

microfluidic device was printed in several blocks. Firstly, the array of the posts was printed in two different blocks but after some unsuccessful printing and development procedures, the printing condition was changed, and the entire post array was printed in a single block. Moreover, while creating the job file several printing parameters were adjusted to improve the printing condition. In addition, new IP-S photoresist was used, and the IP-S photoresist was stored at 4 ºC temperature for further use. After changing the parameters, a satisfactory change was observed in the printing and development process and an improved Device_D was obtained. Figure 4.3 demonstrated a fluorescence image depicting the array of posts in an improved version of Device_D. As shown in Figure 4.3, fewer imperfections or non-developed photoresists were evident between the posts.

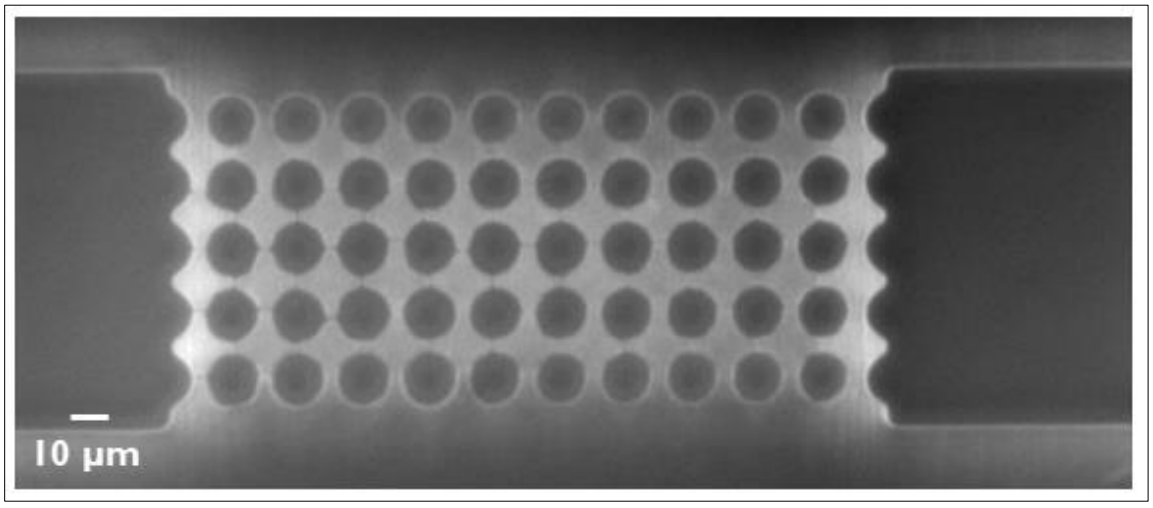

Figure 4.3: Fluorescence image of an improved version of Device_D. Fewer imperfections were observed.

After successfully printing and developing several Device_D, the devices were used for performing dielectrophoretic experiments with protein. For performing dielectrophoretic experiments, the 3D printed microfluidic devices were cleaned with the

buffer solution several times and then the channel of the microfluidic device was filled with protein sample. During the filling process, bubbles were formed inside the post array of the channel of the microfluidic device as demonstrated in Figure 4.4(a).

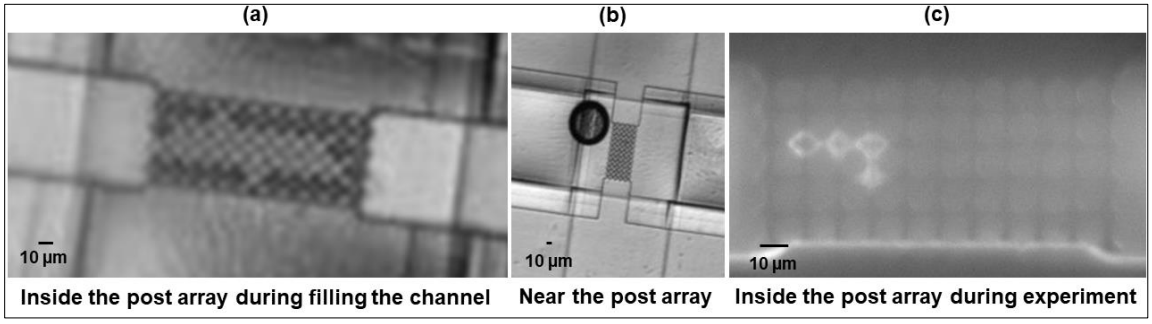

Figure 4.4: Brightfield and fluorescence images of the rectangular channel device with horizontal and vertical post-to-post gap of 5 µm (Device_D) before and during performing dielectrophoretic experiments with proteins. Bubbles were formed (a) inside the post while filling the microfluidic channel before performing the dielectrophoretic experiments, (b) near the post during performing the dielectrophoretic experiments, and (c) inside the post during performing the dielectrophoretic experiments.

Moreover, during performing the dielectrophoretic experiments, when the potential was applied, bubbles were formed near the post array or at the edge of the rectangular constriction as demonstrated in Figure 4.4(b) and inside the post array as demonstrated in Figure 4.4(c). Due to the formation of bubbles, the dielectrophoretic experiments were hindered several times and no reproducible results were obtained. One of the foremost reasons for the formation of bubbles during the filling process and during the dielectrophoretic experiment using the Device_D was the 90^{o} angle in the rectangular constriction of the Device_D. Due to the 90^{o} angle in the rectangular constriction of the Device_D, the flow of the protein sample was restricted and initiated the formation of bubbles. Moreover, when higher potential was applied during dielectrophoretic experiments, the formation of bubbles was increased.

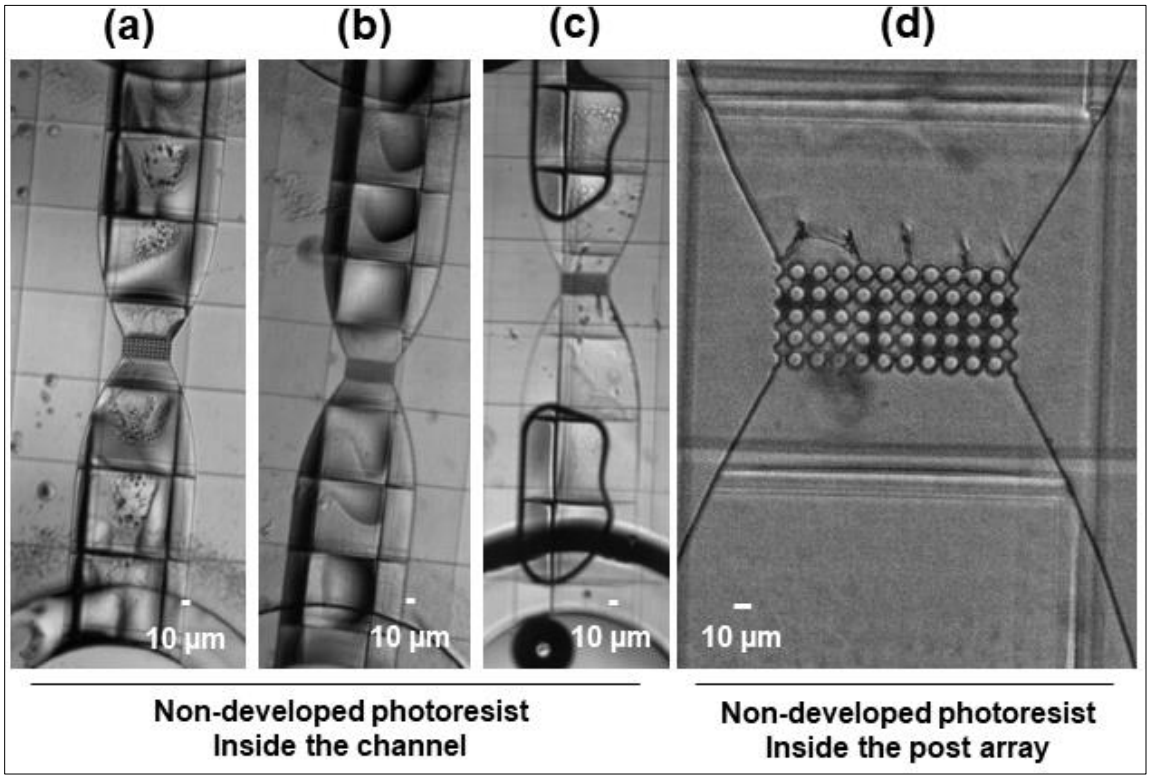

Figure 4.5: Brightfield images of the imperfect Device_F after printing and development. (a), (b), (c) non-developed photoresist inside the channel, and (d) non-developed photoresist inside the post array after the printing and development process.

To overcome the bubble issue during the filling process and during the dielectrophoretic experiment, the 90^{o} angle in the rectangular constriction of the design of Device_D was modified. The 90^{o} angle in the rectangular constriction was converted into a curved constriction (Device_F) so that the protein sample could flow toward the post array without any restriction. Afterward, the Device_F was printed using the 2PP 3D printing technique and developed using a similar procedure as discussed in Section 4.1. Nonetheless, after printing and development, the Device_F was not properly developed initially. Non-developed photoresist remained as demonstrated in Figures 4.5(a), 4.5(b),

and 4.5(c). Furthermore, the post array of the Device_F was not properly developed and, there was non-developed photoresist remaining as demonstrated in Figure 4.5(d).

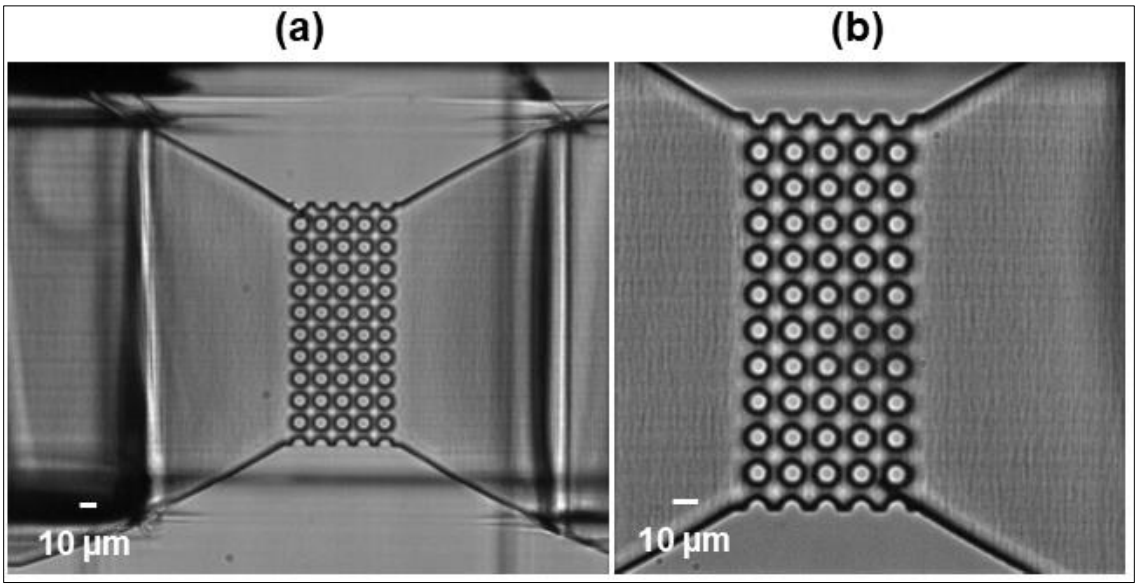

Figure 4.6: Brightfield images of a properly developed curved channel device (Device_F). (a) the microfluidic channel was properly developed, and (b) the post array was properly developed. No imperfections were observed.

To solve the challenges during the printing and development process of Device_F and to obtain a properly developed device, some parameters were adjusted. Firstly, a tunnel-like structure was designed within the channel of the microfluidic device to facilitate increased flow of the SU-8 developer through the channel and the post array, ensuring efficient development of the photoresist. Some printing parameters were changed while creating the job file from the STL file using Describe software for better printing features of the 3D printed microfluidic device. Moreover, a parameter sweep study was performed using the post array section of the design of the microfluidic device to obtain the proper laser power and scan speed for getting properly printed and developed devices. For the parameter sweep study, 50000 µm/s, 60000 µm/s, 80000 µm/s, 100000 µm/s and 120000

µm/s scan speed and 30%, 40%, 50%, 60%, 80%, 90% and 100% laser power were used accordingly. The result of the parameter sweep study demonstrated that when for contour writing the laser power of 80%, and the scan speed of 50000 µm/s was used and further, for solid hatch lines writing the laser power of 60%, and the scan speed of 60000 mm/s was used the post array of the microfluidic device was properly printed and developed. Therefore, for further printing of the Device_F, these parameters were employed. In addition, during the printing of Device_F, a fresh batch of IP-S photoresist stored at 4 ^{o}C was utilized. After printing the microfluidic device, a rigorous development procedure was performed with the SU-8 developer using a vacuum and repeated several times to completely remove the non-developed photoresist inside the post array and channel of the microfluidic devices. After adjusting all the parameters for the printing process and after rigorous development, a well-developed Device_F was obtained successfully as demonstrated in Figures 4.6(a) and 4.6(b). The channel and the post array of Device_F were properly developed, and no excess photoresists remained inside the channel and post array section. Subsequently, the properly printed and developed Device_E and Device_F were utilized for performing dielectrophoretic experiments to explore the dielectrophoretic characteristics of nanometer-sized proteins.

CHAPTER 5

INSULATOR-BASED DIELECTROPHORETIC MANIPULATION OF NANOMETER-SIZED PROTEINS

Currently, protein dielectrophoresis (DEP) is at a crucial phase. A theoretical model for explaining protein DEP supported by molecular dynamic simulations of solvated proteins was provided by Matyushov et al[15]. However, this theoretical model has not been universally applicable and accepted till now, and furthermore, this theoretical model has yet to be experimentally verified. Moreover, as per the recent study by Colburn and Matyushov[12], according to the CM polarization model, the $\boldsymbol{\nabla E^2}$ required to manipulate proteins using DEP was approximately on the order of ~4×10^{21} V^2/m^3. However, as per the literature review, various scientists demonstrated the trapping of smaller proteins using electrode-based DEP and insulator-based DEP at a very low $\boldsymbol{\nabla E^2}$ value[10, 40] sometimes down to 10^{12} V^2/m^3. The likely reason behind this is, in DEP experiments, both the permanent and induced dipole moments of the protein are considered, while the CM polarization theory solely considers the induced ones. In the recently published article, Colburn and Matyushov[12] introduced a dipolar mechanism to estimate the DEP force for proteins, taking into account both the permanent and induced dipole moments of the protein. According to the dipolar mechanism, the estimated $\boldsymbol{\nabla E^2}$ required for capturing proteins is on the order of 10^{17} V^2/m^3.[12]

Ferritin which is an iron-storage nm-sized spherical core-shell protein was used in this study to explore protein dielectrophoretic characteristics. Ferritin has two components; one is the ferrihydrite ($5Fe_2O_3 \cdot 9H_2O$) core and another one is the apoferritin shell[11]. Ferritin is comprised of 24 subunits. Two types of subunits are present; the heavy (H)

subunit with a molecular weight of 21 kDa and the light (L) subunit with a molecular weight of 19 kDa[11]. The molecular weight of ferritin is 440 kDa. The dielectrophoretic characteristics of labeled ferritin were explored and correlated in both the Device_A (straight channel device with horizontal gap of 20 µm and vertical gap of 10 µm) which generated the lowest ∇E^2 (2.28 x 10^{16} V^2/m^3) among all the six designs and in the Device_D (rectangular channel device with both the horizontal and vertical gap of 5 µm) which generated the highest ∇E^2 (2.79 x 10^{17} V^2/m^3) among all the six designs.

5.1 Methods

5.1.1 Chemicals

4-(2-hydroxyethyl)piperazine-1-ethanesulfonic acid (HEPES), poly(ethylene glycol)-block-poly(propylene glycol)-block-poly(ethylene glycol) (Pluronic® F108) and sodium hydroxide (NaOH) were obtained from Sigma-Aldrich (St. Louis, MO, USA) for the preparation of HEPES buffer containing F-108. The protein sample ferritin (equine spleen – Type I, Saline Solution) was obtained from Sigma-Aldrich (St. Louis, MO, USA). Fluorescein-5-isothiocyanate (FITC 'Isomer I') was obtained from Invitrogen and dimethyl sulfoxide (DMSO) was obtained from Sigma-Aldrich (St. Louis, MO, USA). Deionized (DI) water was obtained from an Elga water purification system (Woodridge, USA). SYLGARD® 184 silicone elastomer kit for polydimethylsiloxane (PDMS) was obtained from Dow Corning Corporation (Midland, MI, USA). Microscope glass slides (Cover glass, No.1 Thickness - 24 x 40 mm) were obtained from Thermo Fisher Scientific (Waltham, MA, USA). Platinum wire with a diameter of 0.1 mm was obtained from

Thermo Fisher Scientific (Waltham, MA, USA). IP-S photoresist was obtained from Nanoscribe (GmbH, Germany) and SU-8 2020 developer was obtained from Kayaku Advanced Materials (Westborough, MA, USA).

5.1.2 Sample Preparation and Labelling Procedure of Ferritin

5.1.2.1 Preparation of HEPES Buffer Solution

Firstly, 0.06 g HEPES was added to the beaker. Then, around 23 mL of deionized water was added to the same beaker. After that, the beaker containing HEPES, and deionized water was placed on the top of a magnetic stirrer and the solution was mixed for about 10 min. The pH of the solution was measured using a pH meter and the pH was 6.8. The pH was then adjusted using 1M NaOH solution to the final pH of 7.4. Afterward, 0.37 g Pluronic F-108 was added to the same solution to make the concentration of Pluronic-F-108 1 mM, and the solution was mixed for about 30 min. Then, the solution was transferred to a volumetric flask and further DI water was added to make the total volume 25 mL. Furthermore, the 10 mM HEPES containing 1 mM Pluronic F-108 buffer solution was filtered using a 0.2 µm PTFE membrane filter. The prepared 10 mM HEPES containing 1 mM Pluronic F-108 buffer solution was transferred from the volumetric flask to the glass vial.

5.1.2.2 Preparation of $NaHCO_3$ (Sodium Bicarbonate) Buffer Solution

Firstly, 0.13 g $NaHCO_3$ was added to the beaker. Then, around 14 mL of deionized water was added to the same beaker. After that, the beaker containing $NaHCO_3$, and

deionized water was placed on the top of the magnetic stirrer and the solution was mixed for about 10 min. The pH of the solution was measured using a pH meter and the pH was 8.6. The efficiency of the labeling reaction of ferritin protein with fluorescein isothiocyanate (FITC) is higher at pH 9.00. For this reason, the pH of the solution was adjusted using 1 M NaOH solution to find a pH of 9.0. Furthermore, the 0.1 M $NaHCO_3$ buffer solution was filtered using a 0.2 µm PTFE membrane filter. Then, the solution was transferred to a volumetric flask and further DI water was added to make the total volume 15 mL. The prepared 0.1 M $NaHCO_3$ buffer solution was transferred from the beaker to the glass vial.

5.1.2.3 Labelling Procedure of Ferritin with Fluorescein Isothiocyanate (FITC)

15.6 mg Fluorescein Isothiocyanate (FITC) were transferred to an Eppendorf tube. Then, 2 mL DMSO solvent was added to the same Eppendorf tube. The whole solution was mixed using a pipette for around 2 min. The whole process was performed in the dark through wrapping the vial with foil. In the second step, from the 20 mM of 2 mL FITC dye solution in DMSO, 100 aliquots of 2 mM of 20 µL were prepared and stored at -20 º C.

At first, 100 µL of 0.1 M $NaHCO_3$ buffer solution was transferred to an Eppendorf tube. Then, 8.50 µL of ferritin solution was added to the same Eppendorf tube. The solution was properly mixed using a pipette, resulting in a ferritin stock solution that was 11.5 µM. All the steps of the reaction were performed in dark conditions.

To prepare labelled ferritin, 5 µL of the 20 mM FITC stock solution in DMSO was added to the same Eppendorf tube. The solution was properly mixed using a pipette. Furthermore, to complete the reaction, the solution was incubated using an 'UltraRocker'

at room temperature at 120 rpm for 6 to 7 hours. Then, the solution was incubated in the fridge for around 12 hours. All steps of the reaction were performed in dark conditions.

To remove excess dye, a 30 kDa centrifuge cut-off filter was placed inside the Eppendorf tube. Then, the 30 kDa centrifuge cut-off filter was filled with the labeled ferritin solution and 10 mM HEPES containing 1 mM Pluronic F-108 solution. The Eppendorf tube was placed inside the microcentrifuge and centrifuged for 15 min at 14000 rpm speed and at 4 ^{o}C. The centrifugation steps were repeated around 10 times. Then, the 30 kDa centrifuge cut-off filter containing the labeled ferritin solution was flipped in an Eppendorf tube and centrifuged for 15 min at 4 ^{o}C and 14000 rpm speed to recover the labelled ferritin.

After preparation of the labeled ferritin solution, the solution was buffer exchanged. 100 µL of 10 mM HEPES containing 1 mM Pluronic F-108 buffer solution was added to the Eppendorf tube containing the labeled ferritin solution and the solution was mixed properly using a pipette. Thus, the labeled ferritin in 10 mM HEPES containing 1 mM F108 buffer solution was prepared.

5.1.3 Measurement of Size Distribution and Zeta Potential of the Unlabeled and Labeled Ferritin

Dynamic light scattering technique was used to determine the size distribution and the surface charge of the unlabeled and labeled ferritin with a Zetasizer Ultra (Malvern Panalytical) instrument. 990 µL of 10 mM HEPES containing 1 mM Pluronic F-108 buffer solution was added to two different Eppendorf tubes. In one Eppendorf tube, 10 µL of unlabeled ferritin solution was added and in another Eppendorf tube, 10 µL of labeled

ferritin solution was added. Both solutions were mixed properly using a pipette. The prepared unlabeled and labeled ferritin samples were transferred into a folded capillary cell (DTS1070, Malvern Panalytical) for the size distribution and the zeta potential analysis. Three trials were performed, and the average size distribution value and the average ζ potential value were determined.

5.1.4 Fabrication of PDMS Microfluidic Devices

For designing the microfluidic device layout containing a circular post array, AutoCAD software (Autodesk, San Rafael, CA, USA) was used. The length of the PDMS channel from one reservoir to another reservoir was 1.5 cm, the diameter of the reservoir was 2 cm, and it had a post array containing circular shaped constrictions which had a diameter of 10 μm. The vertical gap was 10 μm, and the horizontal gap was 20 μm. A chrome mask (Advance Repro-duction, North Andover, MA, USA) was purchased and the microfluidic chip layout designed using AutoCAD software was transferred into it. Subsequently, the chrome mask was utilized for the fabrication of a silicon master wafer (University Wafer, South Boston, MA, USA). This process involved patterning structures using the negative photoresist SU-8 through photolithography, employing appropriate exposure and development procedures. Shortly, a 15 μm thick layer of SU-8 2020 photoresist was spin-coated on a 4´´ silicon wafer and then, it was exposed by using UV light through the photomask using the Suss MJB4 Mask Aligner (Suss MicroTech, Germany). Afterwards, the photoresist on top of the silicon wafer was developed using SU-8 developer and baked for 30 min at 150 ^{o}C before use. Afterwards, the silanization process was performed where the silicon wafer was first washed with isopropyl alcohol. Then 40

μL of tridecafluoro-1, 1, 2, 2-tetrahydrooctyl trichlorosilane was added into a weighing boat and both were placed inside a vacuum desiccator for 40 min. Using this silicon wafer a PDMS mold was prepared.

In short, liquid PDMS and PDMS curing agent were blended in a 10:1 (w/w) ratio for around 2 min with continuous stirring. The mixture was slowly poured onto a petri dish containing silicon wafer. Then, the petri dish was placed inside the vacuum desiccator for around 40 min for the degassing process. Then, the mixture was placed inside the oven overnight at 80 ^{o}C for the curing process. The next day, the PDMS mold was removed from the master wafer and the Petri dish carefully. The PDMS slab was sliced into relevant dimensions, and a 2 mm puncher was used to create the reservoirs at the start and end of the post array of the microfluidic channel. The PDMS slabs were washed with isopropyl alcohol and dried with a flow of nitrogen gas. To activate the surface of the PDMS slab and the thin glass slide, an oxygen plasma exposure with a PDC-001, Harrick Plasma cleaner Harrick, USA at high RF (18 W) was used for 2 min. The PDMS slab was immediately pressed on top of the glass slide after the plasma treatment to form a closed microchannel. Then, to prevent non-specific adsorption during the dielectrophoretic experiments, the surface of the microchannel was coated with 1 mM Pluronic F108 solution in water and incubated in a 100% humid environment overnight.

5.1.5 Experimental Setup for Dielectrophoretic Measurements and Procedure of Imaging

The PDMS microfluidic device and the 3D printed microfluidic device were cleaned with 10 mM HEPES containing 1 mM F-108 buffer solution before starting the

dielectrophoretic experiment. Thin platinum electrodes (0.1 mm) were placed into the two reservoirs of the 3D printed microfluidic device. The reservoirs were then filled with the labeled ferritin sample. The microchips were secured on the microscope stage, and the Pt electrodes were connected via electrode micro clamps (Labsmith, Livermore, CA, USA) to an amplifier that provided high voltage (AMT-3B20, Matsusada Precision Inc.). The AC signal was produced using a USB 6343 DAQ device (USB X series, National Instrument, TX, USA) and programmed by LabVIEW 2014, version 14.0. Fluorescence imaging of the labeled ferritin was obtained using an inverted microscope (IX71, Olympus, Center Valley, PA, USA) equipped with a 100 W mercury burner (U-RFL-T, Olympus, Center Valley, PA, 54 USA). The images were visualized with 20x and 40x objectives. Images were taken using a monochromatic QuantEM:512SC CCD camera (Photometrics, Tucson, AZ, USA) and Micro-Manager software (version 1.4.9, Vale Lab, UCSF, CA, USA). Exposure time was varied from 10 ms to 50 ms for capturing the images. A filter set containing a 470/40 nm exciter and a 511/40 nm emitter was used to narrow the wavelength of fluorescence excitation and emission and to image the fluorescence from the labeled ferritin sample. Recorded images and videos were processed by ImageJ software (version 1.54).

5.2 Results

5.2.1 Characterization of the Unlabeled and Labeled Ferritin

To study the dielectrophoretic characteristics of ferritin, the non-fluorescent ferritin protein was labeled with a fluorescent dye, FITC as described in Section 5.1.2.3. During the labeling reaction, the isothiocyanate (–N=C=S) group in the FITC bonds to

nucleophiles, for instance, the -NH_2 group or the –SH group present in the protein. There are three different sites in which FITC used to bond with protein: (i) with the primary amino group at the N-terminal side of the proteins, (ii) with sulfhydryl targeting cysteine side chains in the proteins, and (iii) with the amino groups present in the side chain of peptides or proteins.[41, 42, 43, 44]

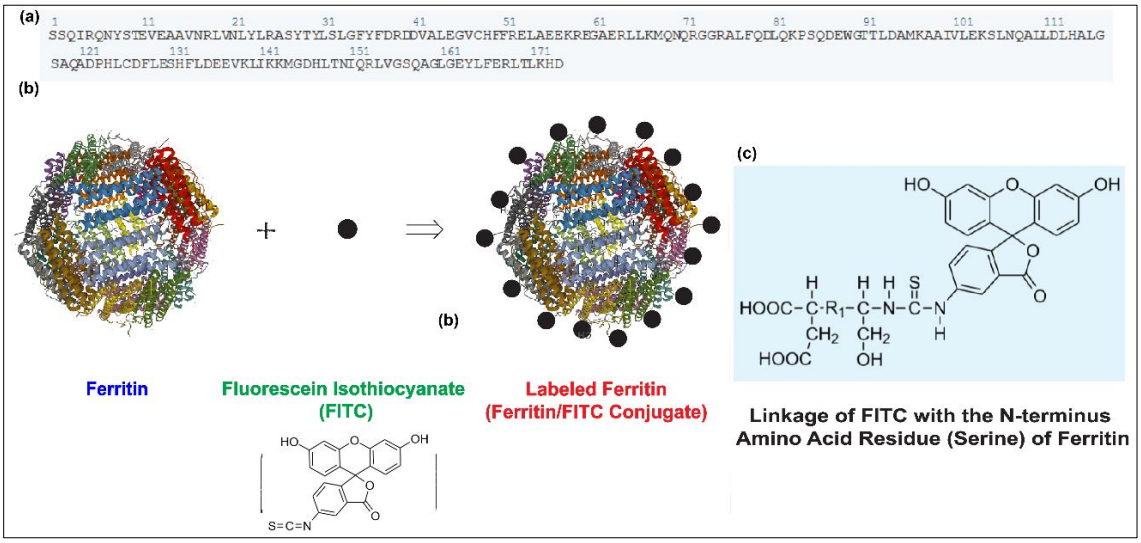

Figure 5.1: (a) The amino acid sequence of ferritin (equine spleen_PDB ID - 1IER), (b) Schematic representation of the labeling reaction of ferritin with FITC and, (c) Possible linkage of FITC (i) with the N-terminus amino acid residue (Serine) of ferritin.

The amino acid sequence of ferritin was illustrated in Figure 5.1(a) [https://doi.org/10.2210/pdb1IER/pdb]. The schematic representation of the labeling reaction of ferritin with FITC was illustrated in Figure 5.1(b). Moreover, the most possible linkage of FITC with ferritin was shown in Figure 5.1(c) [41, 42, 43, 44]. As shown in Figure 5.1(a), serine is the N-terminus amino acid in ferritin. The N-terminus is the start of the polypeptide chain of a protein, and it also refers to the presence of a free amine group (-NH_2) at one end of the polypeptide chain. The free -NH_2 group at the one end of the polypeptide chain of ferritin is more prone to bond with the –N=C=S group in the FITC

and this is referred as the primary reaction for the labeling process of ferritin with FITC. The primary -NH_2 group at the N-terminal side of serine reacted with the –N=C=S group in FITC[41, 42, 43, 44] as illustrated in Figure 5.1(c).

The size distribution and zeta potential of the labeled ferritin were analyzed using dynamic light scattering to determine the size and surface charge of the labeled ferritin.

5.2.1.1 Analysis of the Size Distribution of the Unlabeled and Labeled Ferritin

The size distribution plot for unlabeled ferritin was illustrated with two peak average hydrodynamic diameters (D_h): one at 17.00 ± 0.36 nm [Figure 5.2 (a) and (b)] and another at 490.17 ± 193.39 nm [Figure 5.2 (b)].

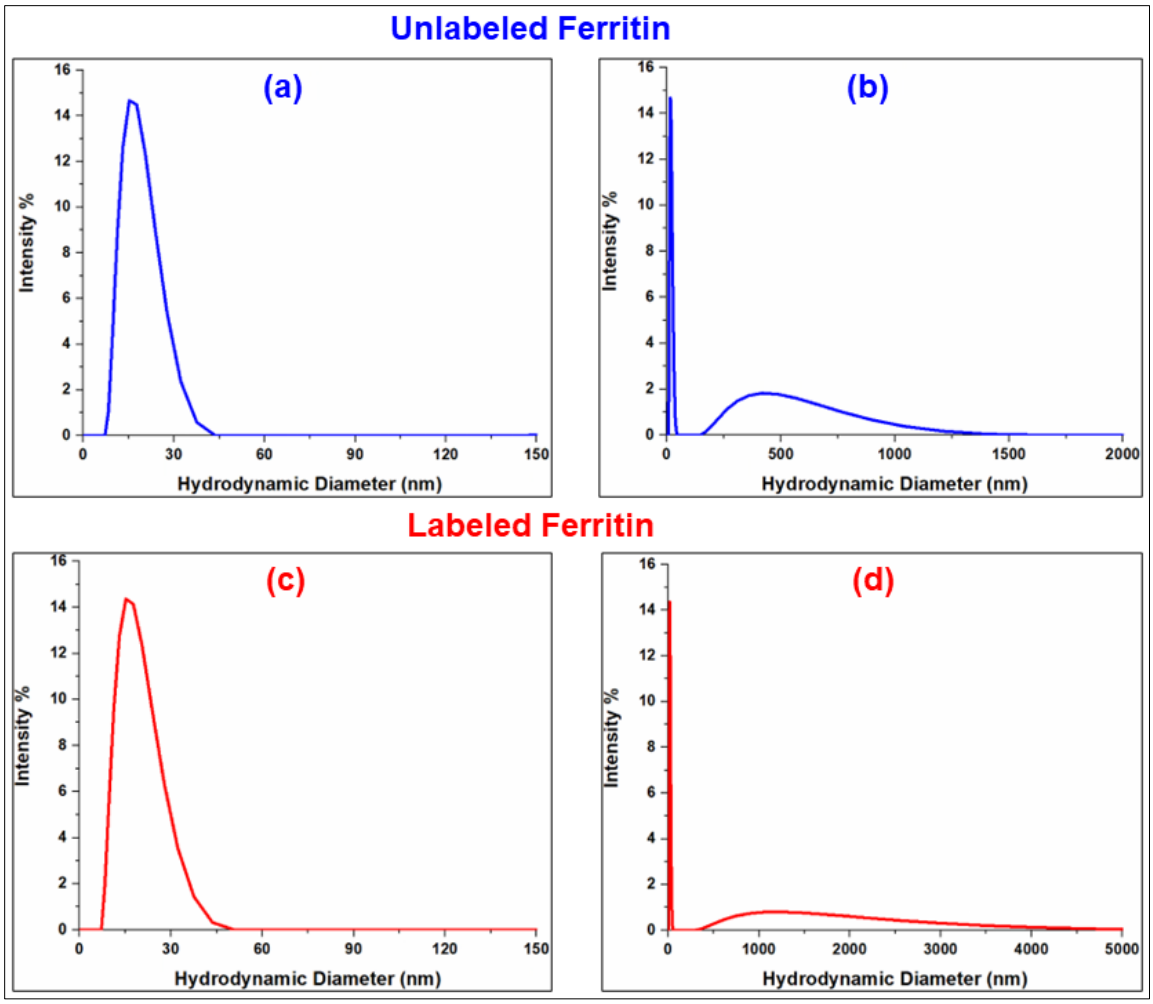

Figure 5.2: Size distribution plot of (a, b) unlabeled ferritin, and (c,d) labeled ferritin in 10 mM HEPES.

The peak at 17.00 ± 0.36 nm indicated the existence of unlabeled ferritin and the peak at 490.17 ± 193.39 nm indicated the existence of impurities in the 10 mM HEPES solution. According to theoretical simulation[25], ferritin has an outer diameter of approximately 12 nm. The core size is approximately 8 nm large. Moreover, the thickness of the apoferritin shell is ~2.3 ± 0.4 nm[25]. The experimental results were in good agreement with the theoretical results. The size distribution plot for labeled ferritin was illustrated

with two peak average D_h: one at 17.68 ± 0.35 nm [Figure 5.2 (c)] and another at 1552.53 ± 39.95 nm [Figure 5.2 (d)]. The peak at 17.68 ± 0.35 nm indicated the existence of labeled ferritin and the peak at 1552.53 ± 39.95 nm indicated the existence of impurities in the 10 mM HEPES solution. The D_h for labeled ferritin was slightly higher in comparison with the D_h for unlabeled ferritin which was an indication of the successful labelling of ferritin. Moreover, it also indicated that a single monomeric form of labeled ferritin was present in the solution[45].

5.2.1.2 Analysis of the Zeta Potential of the Unlabeled and Labeled Ferritin

The zeta potential (ζ) plots for unlabeled and labeled ferritin were illustrated in Table 5.1. The ζ values with standard deviation for the unlabeled ferritin was - 17.67 ± 1.04 mV and for the labeled ferritin was - 14.37 ± 1.04 mV. There was a slight increment in the ζ value for the labeled ferritin in comparison with the unlabeled ferritin. Some previous zeta potential research on proteins[46] demonstrated that the negatively charged amino acids of protein exist in two domains.

One is the Z-domain which contains a higher number of charged amino acids compared to the GA-domain which contains a lower number of charged amino acids, respectively[45]. After labeling, there were negatively charged FITC dye molecules attached to ferritin which may induce more negative charges in labeled ferritin. However, it was possible that the negatively charged amino acids of the Z-domain were shielded to a larger extent and thus there was a slight increment of the ζ potential value for labeled ferritin[46].

5.2.2 Dielectrophoretic Characterization of Ferritin Using Device_A

The dielectrophoretic characteristics of labeled ferritin were studied experimentally using Device_A. From the result of the COMSOL simulations discussed in Section 3.2.2, it was demonstrated that Device_A generated the lowest ∇E^2 among all six designs which was 2.28 x 10^{16} V^2/m^3 when the applied electric field was 1000 V/cm. The experimental setup of the DEP experiment with Device_A was discussed in Sections 5.1.4 and 5.1.5 and was shown in Figure 5.3.

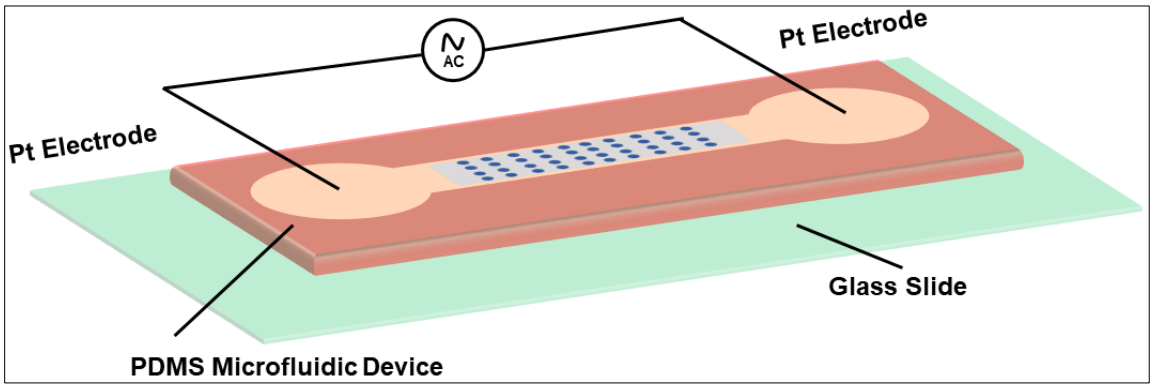

Figure 5.3: Schematic illustration of the experimental setup of the DEP experiment with the PDMS microfluidic device.

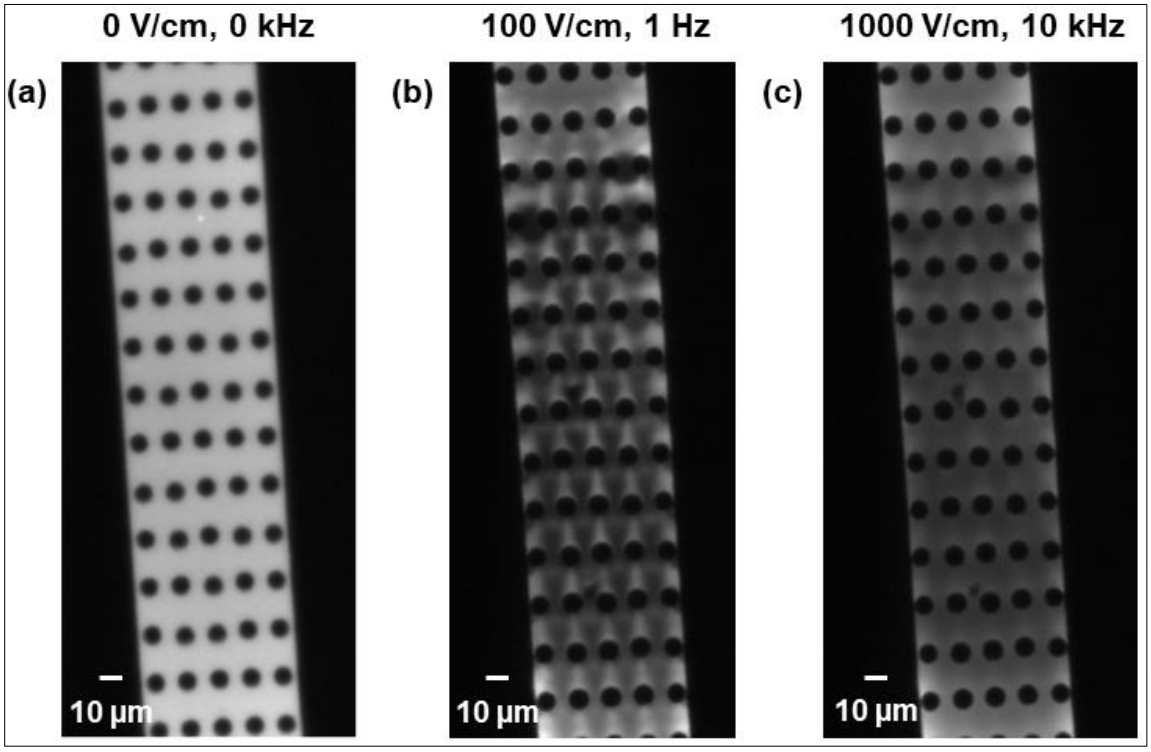

Figure 5.4: Fluorescence imaging of labeled ferritin subject to explore the DEP characteristics in the conventional PDMS microfluidic device. (a) without applied potential 0 V, no trapping was observed, (b) with applied potential 150 V (100 V/cm, 1 Hz), steaming DEP characteristic in pDEP mode was observed, and (c) with applied potential 1500 V (1000 V/cm, 10 kHz), no trapping was observed.

During the dielectrophoretic experiment, a range of potentials and frequencies was applied across the microfluidic channel. Figure 5.4(a) illustrated the fluorescence microscopic image of the microfluidic channel without applying potential. From the experimental observation, it can be stated that no dielectrophoretic characteristic was observed in this condition.

The fluorescence microscopic image of the microfluidic channel of the Device_A with an applied potential of 150 V (100 V/cm) and applied frequency of 1 Hz was illustrated in Figure 5.4(b). Interestingly, the experimental observation demonstrated streaming DEP characteristics for labeled ferritin which referred to the focusing of proteins

into streams by equilibrating the dielectrophoretic and electrokinetic forces acting on them[38]. Nakano et al.[6] demonstrated a numerical simulation and experimental observation using elliptical posts containing PDMS microfluidic devices for the analysis of small proteins.

Nakano et al.[6] used DC potential in the numerical simulation and throughout the dielectrophoretic experiment and the result showed that when streaming DEP in pDEP mode occurred, the maximum concentration was created along the posts. When streaming DEP in nDEP mode occurred, the very same regions become depleted[5]. Remarkably, Cummings et al.[47, 39] investigated that the streaming DEP characteristics and concentration behavior occur when DEP overcomes diffusion but is too weak to overcome the electrokinetic flow. Accordingly, when we applied a potential of 150 V (100 V/cm) and frequency of 1 Hz, the protein molecules moved back-and-forth which almost resembled the DC potential case. It can thus be stated that the labeled ferritin exhibited streaming DEP characteristics in pDEP mode when 150 V (100 V/cm) potential and 1 Hz frequency were applied. Therefore, labeled ferritin proteins overcame diffusion but were unable to overcome the electrokinetic flow, wherein the electrokinetic forces (including electrophoretic force and electroosmotic force) proved to be more dominant forces than the DEP force[47, 39].

As illustrated in Figure 5.4(c), the fluorescence microscopic image with an applied potential of 1500 V (1000 V/cm) and applied frequency of 10 kHz didn't demonstrate any streaming DEP characteristics.

It can be concluded that when a potential of 150 V (100 V/cm) and frequency of 1 Hz was applied, the $\boldsymbol{\nabla E^2}$ was 2.28 x 10^{14} V^2/m^3 and the $\boldsymbol{\nabla E^2}$ is not enough to observe

trapping of ferritin proteins using low-frequency insulator-based DEP. As a result, labeled ferritin proteins overcame diffusion but did not overcome the electrokinetic flow and thus streaming DEP characteristics were observed. Moreover, the electrokinetic forces (electrophoresis force and electroosmosis force) are more dominant forces than the DEP force, and thus no trapping of ferritin proteins was observed. Additionally, when the potential of 1500 V (1000 V/cm) and frequency of 10 kHz was applied, the $\boldsymbol{\nabla E^2}$ was 2.28 x 10^{16} V^2/m^3 and the $\boldsymbol{\nabla E^2}$ is not enough to observe trapping of ferritin proteins using low-frequency insulator-based DEP. Hence, ferritin protein was unable to overcome both the diffusion and electrokinetic flow, and further the electrokinetic forces are more dominant forces compared to the DEP force[47, 39].

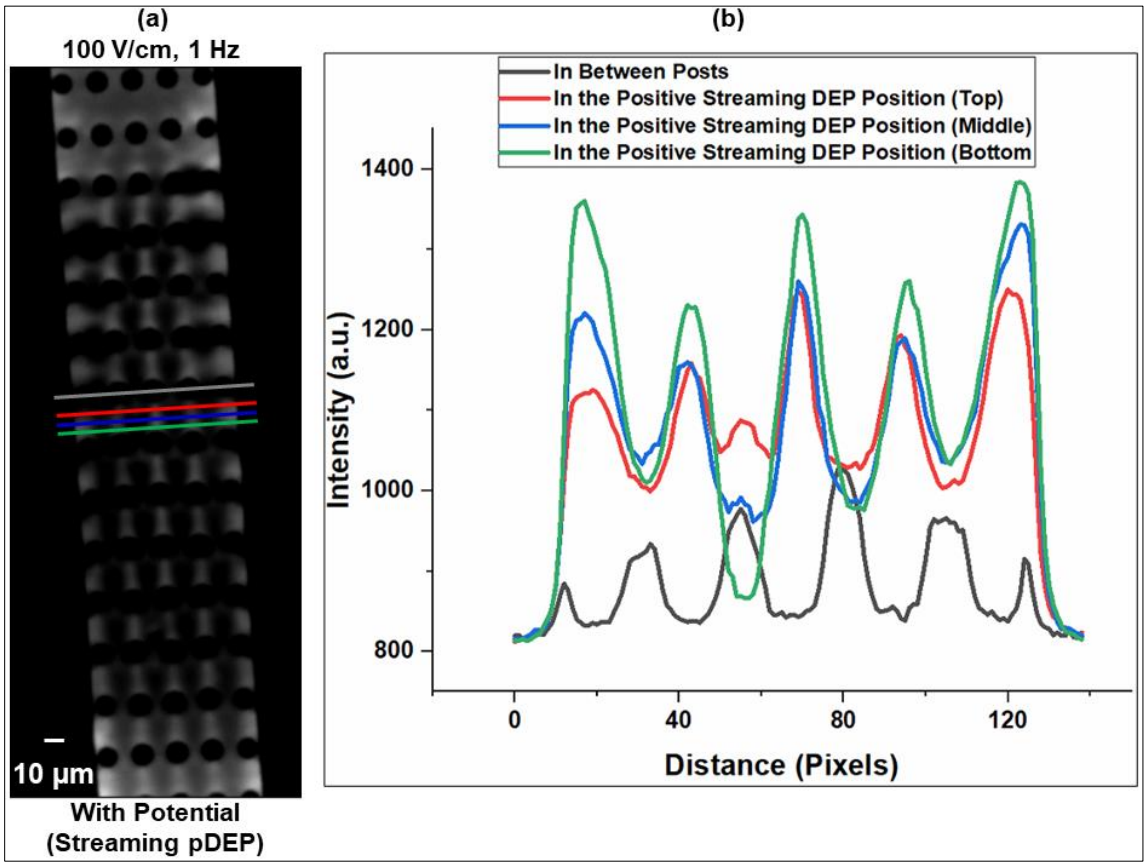

Figure 5.5: Intensity distribution plot of the fluorescence image of labeled ferritin subject to explore the DEP characteristics in Device_A. With applied potential 150 V (100 V/cm, 1 Hz), streaming pDEP characteristic was observed. (a) Position of the lines was depicted in the fluorescence image for plotting the intensity distribution of labeled ferritin, (b) the intensity distribution plot of the fluorescence image of labeled ferritin.

To provide further confirmation of positive streaming DEP behavior of labeled ferritin in the Device_A with lower $\boldsymbol{\nabla E^2}$, an intensity distribution plot was generated from the fluorescence image of labeled ferritin, as depicted in Figure 5.5. Initially, the background was subtracted from the raw image, followed by drawing lines at the desired positions of the fluorescence image. Then, intensity plots were generated. In Figure 5.5(b), the black line depicted the intensity distribution between the posts and the intensity values were decreased at the location of the posts. Furthermore, the red, blue, and green lines denoted the intensity distribution at the positive streaming DEP trapping positions, respectively, and the intensity values were increased directly above the posts. Moreover, Figure 5.5(b) demonstrated that the protein streams' intensity was lower at the immediate bottom of the posts within one row, then there was a slight increase in intensity at the middle of the posts within two rows, reaching its peak at the immediate top of the posts within the subsequent row.

5.2.3 An Outlook of Dielectrophoretic Characterization of Ferritin Using Device_D which Generated the Highest $\boldsymbol{\nabla E^2}$

The dielectrophoretic characteristic of labeled ferritin was studied experimentally using Device_D where the length of the channel from one reservoir to another reservoir was 2.31 mm. From the result of the COMSOL simulations discussed in Section 3.2.2, it

was demonstrated that Device_D generated the highest ∇E^2 among the six designs which was 2.79 x 10^{17} V^2/m^3 when the applied electric field was 1000 V/cm. The experimental setup of the DEP experiment with Device_D was discussed in Sections 5.1.4 and 5.1.5 and was shown in Figure 5.6.

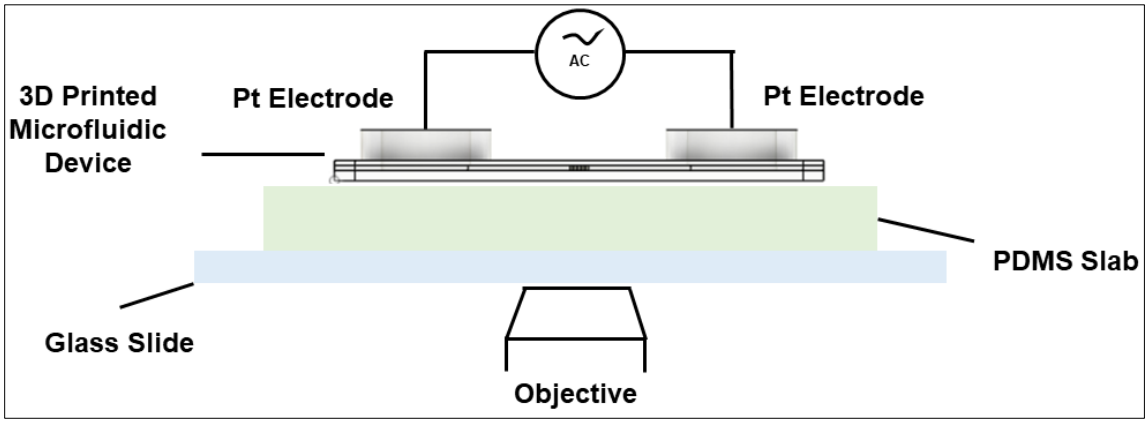

Figure 5.6: Schematic illustration of the experimental setup of the DEP experiment with a 3D printed microfluidic device.

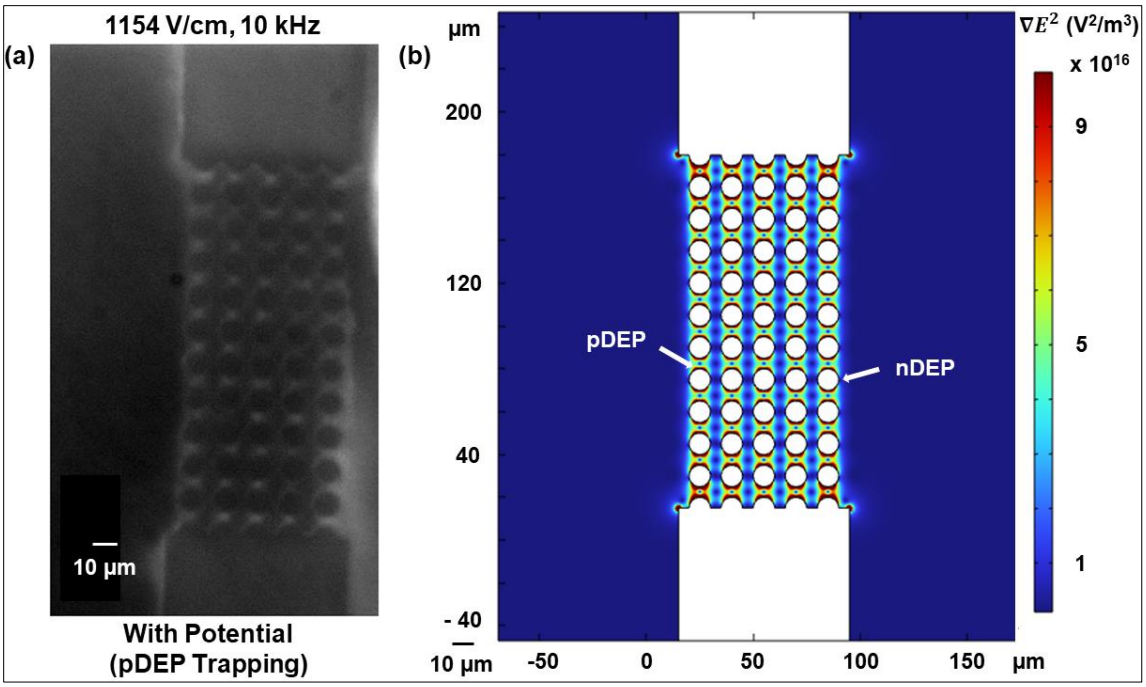

Figure 5.7: (a) Fluorescence imaging of labeled ferritin subject to DEP in the Device_D. With applied potential 300 V (1154 V/cm, 10 kHz), pDEP characteristic was observed. (b) COMSOL simulation of the electric field distribution in the section of the post array of the microfluidic device indicating the region of the lowest and highest electric field.

During the dielectrophoretic experiment in Device_D with higher $\boldsymbol{\nabla E^2}$, a range of potentials and frequencies was applied across the microfluidic channel. In Figure 5.7(a), a fluorescence image during the dielectrophoretic experiment when the applied potential was 300 V (1154 V/cm) and the applied frequency was 10 kHz was illustrated. The labeled ferritin accumulated in the highest electric field regions, exhibiting pDEP characteristics. The DEP force emerged as the predominant force over the electrokinetic forces (including the electrophoretic force and electroosmosis force), resulting in the labeled ferritin protein displaying DEP trapping characteristics.

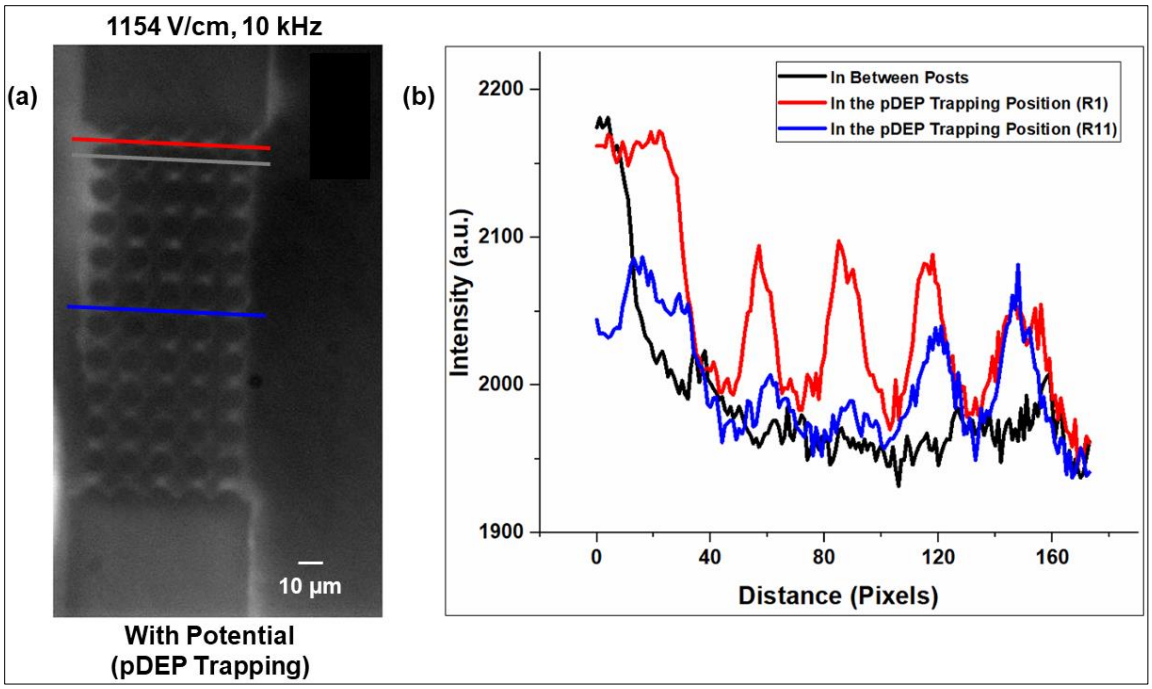

Figure 5.8: Intensity distribution plot of the fluorescence image of labeled ferritin subject to DEP in Device_D. With applied potential 300 V (1154 V/cm, 10 kHz), pDEP characteristic was observed. (a) Position of the lines was depicted in the fluorescence image for plotting the intensity distribution of labeled ferritin and, (b) the intensity distribution plot of the fluorescence image of labeled ferritin. Black line represented the intensity distribution in between the posts, red line represented the intensity distribution in the pDEP trapping position in R1 and blue line represented the intensity distribution in the pDEP trapping position in R11.

To provide additional evidence of pDEP trapping of labeled ferritin in the Device_D with higher $\boldsymbol{\nabla E^2}$, an intensity distribution plot was generated from the fluorescence image of labeled ferritin, as depicted in Figure 5.8. Initially. the background was subtracted from the raw image, followed by drawing lines at the desired positions of the fluorescence image. Then, intensity plots were generated. In Figure 5.8(b), the black line delineated the intensity distribution between the posts and the intensity values were diminished at the location of the posts. Furthermore, the red and blue lines denoted the intensity distribution at the positions of pDEP trapping for R1 and R11, respectively and

the intensity values were elevated directly above the posts. The intensity distribution plot provided additional evidence of the pDEP trapping of labeled ferritin in Device_D. Moreover, as demonstrated in Figure 5.8(b), the intensity distribution of trapped labeled ferritin was higher for R1 (red line) compared to the intensity distribution for R11 (blue line). As discussed in Section 3.2.3 based on the numerical simulation findings, Device_D indicated that R1 generated the highest $\boldsymbol{\nabla E^2}$, whereas R11 yielded the lowest $\boldsymbol{\nabla E^2}$ among all rows. As a result, the intensity distribution of trapped labeled ferritin was greater for R1, as R1 produced the highest $\boldsymbol{\nabla E^2}$, while the intensity distribution for R11 was lower, given that R11 generated the lowest $\boldsymbol{\nabla E^2}$. Hence, the intensity plot distribution aligned with the numerical simulation results for Device_D.

From the numerical simulation result, the estimated $\boldsymbol{\nabla E^2}$ reached 3.72 x 10^{17} V^2/m^3 when the potential of 300 V (1154 V/cm) and frequency of 10 kHz was applied in Device_D. In this condition, labeled ferritin demonstrated pDEP characteristics. According to the recently derived dipolar mechanism of DEP by Colburn and Matyushov[12], the required $\boldsymbol{\nabla E^2}$ for trapping proteins is in the order of 10^{17} V^2/m^3. Some researchers[48,17,8] also experimentally demonstrated the capture of BSA proteins at a $\boldsymbol{\nabla E^2} \simeq 10^{17}$ V^2/m^3. Therefore, the experimental observation regarding labeled ferritin aligned well with the existing literature.

A recent study by Colburn and Matyushov[12] introduced a model for predicting the DEP force acting on proteins and according to the model the equation for the DEP force is as outlined in chapter 2. Importantly, Colburn and Matyushov[12] elucidated that nDEP characteristics can be observed for submicron and micron size protein aggregates according to the CM induction mechanism. As per the CM induction mechanism, the value of $\chi_{\mathrm{DEP}}^{\mathrm{CM}}$

is negative[11]. The CM induction mechanism becomes dominant for sufficiently large protein aggregates and thus the large protein aggregates exhibited nDEP characteristics[11]. Moreover, pDEP characteristics can be observed for proteins carrying permanent dipole moments according to the dipolar mechanism[11]. As per the dipolar mechanism, the value of $\chi_{\mathrm{DEP}}^{\mathrm{d}}$ is positive from the protein dipole[11]. The dipolar mechanism becomes dominant for proteins carrying permanent dipole moments and thus proteins exhibited pDEP characteristics[11]. The dielectrophoretic experiments performed using labeled ferritin exhibited pDEP characteristics. As per the elucidation presented by Colburn and Matyushov[12], the pDEP trapping characteristics observed in protein dielectrophoretic experiments with labeled ferritin confirmed the entrapment of individual labeled ferritin proteins rather than aggregates thereof.

CHAPTER 6

CONCLUSIONS AND FUTURE PERSPECTIVES

In summary, the objective of this study was to effectively demonstrate strategies to generate higher ∇E^2 in the iDEP microfluidic devices which could be employed for the successful manipulation of nanoscale-sized proteins utilizing the iDEP microfluidic devices. Firstly, numerical simulations were successfully performed which illustrated strategies to generate higher ∇E^2 in the iDEP microfluidic devices. Intriguingly, the numerical simulation results demonstrated that by decreasing the gap in between the posts from 10 μm to 100 nm, the ∇E^2 was increased by ~12 fold. Moreover, the numerical simulation results illustrated that the incorporation of channel constrictions, such as a rectangular constriction (Device_D) or curved constriction (Device_F), a notable increase in ∇E^2 could be achieved. Additionally, the inclusion of rectangular constrictions in the straight channel iDEP device (Device_D) resulted in a greater increase in ∇E^2 compared to the incorporation of curved constrictions in the same device (Device_F). Device_D generated the highest ∇E^2 and Device_F generated the lowest ∇E^2 among all devices. Importantly, the numerical simulation results further illustrated that the straight channel iDEP microfluidic devices generated uniform ∇E^2 across the device, however, the rectangular constrictions or curved constrictions iDEP microfluidic devices generated non-uniform ∇E^2 across the devices.

Subsequently, the numerical simulation results were successfully translated for fabricating the iDEP microfluidic devices. The fabrication of straight channel iDEP microfluidic device (Device_A) with lower ∇E^2 was successfully conducted using the soft lithography technique. Additionally, the fabrication of iDEP microfluidic devices

(Device_D and Device_F) with rectangular and curved constrictions, exhibiting higher ∇E^2, was successfully accomplished using the 2PP 3D printing technique.

This study illustrated the successful labeling of non-fluorescent ferritin protein with fluorescent FITC dye. It further unveiled the dielectrophoretic characteristics of labeled ferritin in Device_A with lower ∇E^2 and in Device_D with higher ∇E^2. Interestingly, in Device_A with lower ∇E^2, the labeled ferritin demonstrated no DEP trapping characteristics. The estimated ∇E^2 was 2.28 x 10^{14} V^2/m^3 when a potential of 150 V (100 V/cm) and frequency of 1 Hz was applied in Device_A, and the ∇E^2 is insufficient to observe trapping of labeled ferritin proteins using low frequency iDEP. Consequently, labeled ferritin proteins overcame diffusion but did not overcome the electrokinetic flow, where the electrokinetic forces are more dominant forces than the DEP force and thus streaming DEP characteristics were observed. Furthermore, the estimated ∇E^2 was 2.28 x 10^{16} V^2/m^3 when the potential of 1500 V (1000 V/cm) and frequency of 10 kHz was applied in Device_A, and labeled ferritin proteins were unable to overcome the diffusion, and the DEP force was not the prevailing force[47, 39] in this scenario. Thus, this magnitude of ∇E^2 is inadequate to observe trapping of labeled ferritin proteins using low frequency iDEP. Importantly, in Device_D with higher ∇E^2, the labeled ferritin demonstrated pDEP trapping characteristics. The estimated ∇E^2 was 3.72 x 10^{17} V^2/m^3 when the potential of 300 V (1154 V/cm) and frequency of 10 kHz was applied in Device_D, and the DEP force became the dominant force and consequently, the labeled ferritin exhibited pDEP characteristics.

There are some future outlooks of the project. The first outlook of this work will be generating ∇E^2 higher than on the order of 10^{17} V^2/m^3 in the 3D printed iDEP microfluidic

devices. One approach to achieve this involved the variation of the horizontal and vertical post-to-post gap. By decreasing the post-to-post gap, $\boldsymbol{\nabla E^2}$ higher than on the order of 10^{17} V^2/m^3 could be generated in the 3D printed iDEP microfluidic devices. Another approach is to increase the size of the reservoir so that high volume of sample can be accommodated in the reservoir. If the sample volume is high in the reservoir than it is feasible to apply higher potential during dielectrophoretic experiments as there is less possibility of the formation of joule heating and thus $\boldsymbol{\nabla E^2}$ higher than could be generated in the 3D printed iDEP microfluidic devices.

The second outlook is to work with new 3D printed devices containing different structured posts. The next attempt is to work with 3D printed devices with cone structured post, dome structured posts and grid structured posts as depicted in Figure 7.1. Interestingly, it is anticipated that the cone, dome, and grid structured posts can generate higher $\boldsymbol{\nabla E^2}$ in comparison to the circular structured posts. Moreover, the printing and development time of the 3D printed devices containing cone, dome, and grid structured posts could be reduced in comparison to the 3D printed devices containing circular structured posts which is a considerable advantage.

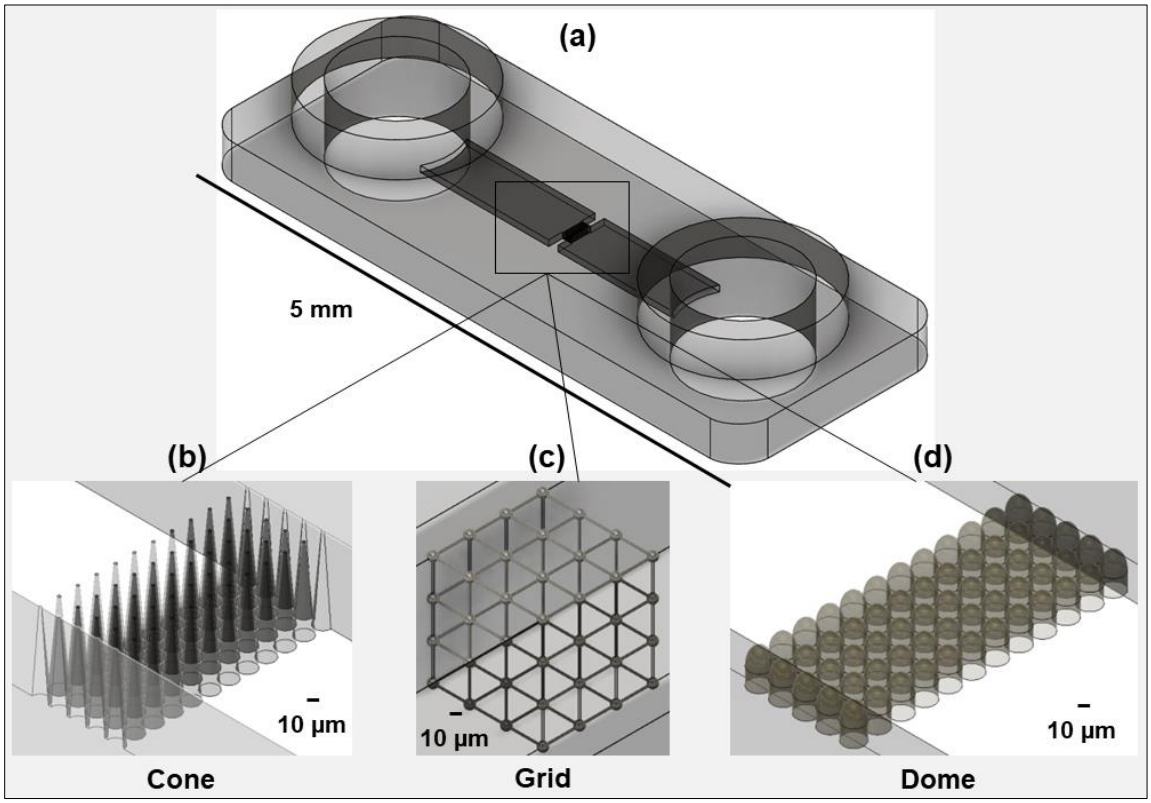

Figure 7.1: 3D Fusion 360 designs of 3D-printed microfluidic device will be employed for iDEP studies of nanometer sized biomolecules. (a) The design of the whole microfluidic device containing circular structured constrictions, and design of different structured constrictions (b) cone, (c) grid, and (d) dome.

Another aim is to work with new proteins. In this work, a spherical shaped protein, ferritin is utilized for exploring the dielectrophoretic characteristics of proteins. A future approach is to work with different shaped proteins e.g. Bovine Serum Albumin (BSA), C-Phycocyanin and Immunoglobulin G.

REFERENCES

(1) Sang, S.; Feng, Q.; Jian, A.; Li, H.; Ji, J.; Duan, Q.; Zhang, W.; Wang, T. Portable Microsystem Integrates Multifunctional Dielectrophoresis Manipulations and a Surface Stress Biosensor to Detect Red Blood Cells for Hemolytic Anemia. *Sci. Rep.* **2016**, *6* (May), 1–8. https://doi.org/10.1038/srep33626.

(2) Whitesides, G. M. The Origins and the Future of Microfluidics. *Nature* **2006**, *442* (7101), 368–373. https://doi.org/10.1038/nature05058.

(3) Zhou, T.; Yeh, L. H.; Li, F. C.; Mauroy, B.; Joo, S. W. Deformability-Based Electrokinetic Particle Separation. *Micromachines* **2016**, *7* (9), 1–10. https://doi.org/10.3390/mi7090170.

(4) Rabbani, M. T.; Schmidt, C. F.; Ros, A. Single-Walled Carbon Nanotubes Probed with Insulator-Based Dielectrophoresis. *Anal. Chem.* **2017**, *89* (24), 13235–13244. https://doi.org/10.1021/acs.analchem.7b03105.

(5) Rabbani, M. T.; Schmidt, C. F.; Ros, A. Length-Selective Dielectrophoretic Manipulation of Single-Walled Carbon Nanotubes. *Anal. Chem.* **2020**, *92* (13), 8901–8908. https://doi.org/10.1021/acs.analchem.0c00794.

(6) Nakano, A.; Chao, T. C.; Camacho-Alanis, F.; Ros, A. Immunoglobulin G and Bovine Serum Albumin Streaming Dielectrophoresis in a Microfluidic Device. *Electrophoresis* **2011**, *32* (17), 2314–2322. https://doi.org/10.1002/elps.201100037.

(7) Ortiz, R.; Koh, D.; Kim, D. H.; Rabbani, M. T.; Anguaya Velasquez, C.; Sonker, M.; Arriaga, E. A.; Ros, A. Continuous Organelle Separation in an Insulator-Based Dielectrophoretic Device. *Electrophoresis* **2022**, *43* (12), 1283–1296. https://doi.org/10.1002/elps.202100326.

(8) Zavatski, S.; Bandarenka, H.; Martin, O. J. F. Protein Dielectrophoresis with Gradient Array of Conductive Electrodes Sheds New Light on Empirical Theory. *Anal. Chem.* **2023**, *95* (5), 2958–2966. https://doi.org/10.1021/acs.analchem.2c04708.

(9) Kim, D.; Sonker, M.; Ros, A. Dielectrophoresis: From Molecular to Micrometer-Scale Analytes. *Anal. Chem.* **2019**, *91* (1), 277–295. https://doi.org/10.1021/acs.analchem.8b05454.

(10) Hölzel, R.; Pethig, R. Protein Dielectrophoresis: I. Status of Experiments and an Empirical Theory. *Micromachines* **2020**, *11* (5). https://doi.org/10.3390/mi11050533.

(11) Kim, M.; Rho, Y.; Jin, K. S.; Ahn, B.; Jung, S.; Kim, H.; Ree, M. PH-Dependent Structures of Ferritin and Apoferritin in Solution: Disassembly and Reassembly. *Biomacromolecules* **2011**, *12* (5), 1629–1640. https://doi.org/10.1021/bm200026v.

(12) Colburn, T.; Matyushov, D. V. Trapping Proteins on Nanopores by Dielectrophoresis. *J. Appl. Phys.* **2023**, *133* (16). https://doi.org/10.1063/5.0144564.

(13) Pethig, R. Dielectrophoresis: Status of the Theory, Technology, and Applications. *Biomicrofluidics* **2010**, *4* (2), 1–35. https://doi.org/10.1063/1.3456626.

(14) Hölzel, R.; Pethig, R. Protein Dielectrophoresis: Key Dielectric Parameters and Evolving Theory. *Electrophoresis* **2021**, *42* (5), 513–538. https://doi.org/10.1002/elps.202000255.

(15) Heyden, M.; Matyushov, D. V. Dielectrophoresis of Proteins in Solution. *J. Phys. Chem. B* **2020**, *124* (51), 11634–11647. https://doi.org/10.1021/acs.jpcb.0c09007.

(16) Nakano, A.; Ros, A. Protein Dielectrophoresis: Advances, Challenges, and Applications. *Electrophoresis* **2013**, *34* (7), 1085–1096. https://doi.org/10.1002/elps.201200482.

(17) Hayes, M. A. Dielectrophoresis of Proteins: Experimental Data and Evolving Theory. *Anal. Bioanal. Chem.* **2020**, *412* (16), 3801–3811. https://doi.org/10.1007/s00216-020-02623-7.

(18) Chiou, C. H.; Chien, L. J.; Kuo, J. N. Nanoconstriction-Based Electrodeless Dielectrophoresis Chip for Nanoparticle and Protein Preconcentration. *Appl. Phys. Express* **2015**, *8* (8). https://doi.org/10.7567/APEX.8.085201.

(19) Lapizco-Encinas, B. H.; Ozuna-Chacón, S.; Rito-Palomares, M. Protein Manipulation with Insulator-Based Dielectrophoresis and Direct Current Electric Fields. *J. Chromatogr. A* **2008**, *1206* (1), 45–51. https://doi.org/10.1016/j.chroma.2008.05.077.

(20) Kovarik, M. L.; Jacobson, S. C. Integrated Nanopore/Microchannel Devices for Ac Electrokinetic Trapping of Particles. *Anal. Chem.* **2008**, *80* (3), 657–664. https://doi.org/10.1021/ac701759f.

(21) Au, A. K.; Huynh, W.; Horowitz, L. F.; Folch, A. 3D-Printed Microfluidics. *Angew. Chemie - Int. Ed.* **2016**, *55* (12), 3862–3881. https://doi.org/10.1002/anie.201504382.

(22) Nge, P. N.; Rogers, C. I.; Woolley, A. T. Advances in Micro Fl Uidic Materials , Functions , Integration , and Applications. **2013**.

(23) Beauchamp, M. J.; Nielsen, A. V.; Gong, H.; Nordin, G. P.; Woolley, A. T. 3D Printed Microfluidic Devices for Microchip Electrophoresis of Preterm Birth Biomarkers. *Anal. Chem.* **2019**, *91* (11), 7418–7425. https://doi.org/10.1021/acs.analchem.9b01395.

(24) Sonker, M.; Sahore, V.; Woolley, A. T. Recent Advances in Microfluidic Sample Preparation and Separation Techniques for Molecular Biomarker Analysis: A Critical Review. *Anal. Chim. Acta* **2017**, *986*, 1–11. https://doi.org/10.1016/j.aca.2017.07.043.

(25) Stühn, L.; Auernhammer, J.; Dietz, C. PH-Depended Protein Shell Dis- and Reassembly of Ferritin Nanoparticles Revealed by Atomic Force Microscopy. *Sci. Rep.* **2019**, *9* (1), 1–9. https://doi.org/10.1038/s41598-019-53943-3.

(26) Voldman, J.; Gray, M. L.; Schmidt, M. A. Microfabrication in Biology and Medicine. *Annu. Rev. Biomed. Eng.* **1999**, No. 1, 401–425. https://doi.org/10.1146/annurev.bioeng.1.1.401.

(27) Damodara, S.; Shahriari, S.; Wu, W. I.; Rezai, P.; Hsu, H. H.; Selvaganapathy, R. *Materials and Methods for Microfabrication of Microfluidic Devices*; 2021. https://doi.org/10.1016/B978-0-12-819971-8.00008-1.

(28) Tabeling, P.; Chen, S. *Introduction to Microfluidics*. OUP Oxford: 2005.

(29) Faraji Rad, Z.; Prewett, P. D.; Davies, G. J. High-Resolution Two-Photon Polymerization: The Most Versatile Technique for the Fabrication of Microneedle Arrays. *Microsystems Nanoeng.* **2021**, *7* (1). https://doi.org/10.1038/s41378-021-00298-3.

(30) Waheed, S.; Cabot, J. M.; Macdonald, N. P.; Lewis, T.; Guijt, R. M.; Paull, B.; Breadmore, M. C. 3D Printed Microfluidic Devices: Enablers and Barriers. *Lab Chip* **2016**, *16* (11), 1993–2013. https://doi.org/10.1039/c6lc00284f.

(31) Yazdi, A. A.; Popma, A.; Wong, W.; Nguyen, T.; Pan, Y.; Xu, J. 3D Printing: An Emerging Tool for Novel Microfluidics and Lab-on-a-Chip Applications. *Microfluid. Nanofluidics* **2016**, *20* (3), 1–18. https://doi.org/10.1007/s10404-016-1715-4.

(32) Santos-Hernandez, M.; Recio, I.; Amigo, L. Electrophoresis. *Encycl. Dairy Sci. Third Ed.* **2021**, *2*, 370–381. https://doi.org/10.5005/jp/books/14203_20.

(33) Hayes, J. D., & Stockman, P. K. (1989). Electrophoresis of Proteins And Nucleic Acids: I: Theory. *BMJ: British Medical Journal* **1989**, *299* (6703), 843–846. http://www.jstor.org/stable/29705506.

(34) Alizadeh, A.; Hsu, W. L.; Wang, M.; Daiguji, H. Electroosmotic Flow: From Microfluidics to Nanofluidics. *Electrophoresis* **2021**, *42* (7–8), 834–868. https://doi.org/10.1002/elps.202000313.

(35) Zhang, J.; Chen, K.; Fan, Z. H. *Circulating Tumor Cell Isolation and Analysis*, 1st ed.; Elsevier Inc., 2016; Vol. 75. https://doi.org/10.1016/bs.acc.2016.03.003.

(36) Mortadi, A.; El Melouky, A.; Chahid, E. G.; El Moznine, R.; Cherkaoui, O. Studies of the Clausius–Mossotti Factor. *J. Phys. Stud.* **2016**, *20* (4), 4001-1-4001–4004. https://doi.org/10.30970/jps.20.4001.

(37) Nakano, A.; Camacho-Alanis, F.; Chao, T. C.; Ros, A. Tuning Direct Current Streaming Dielectrophoresis of Proteins. *Biomicrofluidics* **2012**, *6* (3), 1–13. https://doi.org/10.1063/1.4742695.

(38) Henriksson, A.; Neubauer, P.; Birkholz, M. Dielectrophoresis: An Approach to Increase Sensitivity, Reduce Response Time and to Suppress Nonspecific Binding in Biosensors? *Biosensors* **2022**, *12* (10). https://doi.org/10.3390/bios12100784.

(39) Cummings, E. B. Streaming Dielectrophoresis for Continuous-Flow Microfluidic Devices. *IEEE Eng. Med. Biol. Mag.* **2003**, *22* (6), 75–84. https://doi.org/10.1109/MEMB.2003.1266050.

(40) Pethig, R. Protein Dielectrophoresis: A Tale of Two Clausius–Mossottis or Something Else? *Micromachines* **2022**, *13* (2). https://doi.org/10.3390/mi13020261.

(41) Jullian, M.; Hernandez, A.; Maurras, A.; Puget, K.; Amblard, M.; Martinez, J.; Subra, G. N-Terminus FITC Labeling of Peptides on Solid Support: The Truth behind the Spacer. *Tetrahedron Lett.* **2009**, *50* (3), 260–263. https://doi.org/10.1016/j.tetlet.2008.10.141.

(42) Maeda, H.; Ishida, N.; Kawauchi, H.; Tuzimura, K. Reaction of Fluorescein-Isothiocyanate with Proteins and Amino Acids: I. Covalent and Non-Covalent Binding of Fluorescein-Isothiocyanate and Fluorescein to Proteins. *J. Biochem.* **1969**, *65* (5), 777–783. https://doi.org/10.1093/oxfordjournals.jbchem.a129077.

(43) Guedes, S.; Neves, B.; Vitorino, R.; Domingues, R.; Cruz, M. T.; Domingues, P. Contact Dermatitis: In Pursuit of Sensitizer's Molecular Targets through Proteomics. *Arch. Toxicol.* **2017**, *91* (2), 811–825. https://doi.org/10.1007/s00204-016-1714-y.

(44) Jaklová Dytrtová, J.; Moslova, K.; Jakl, M.; Sirén, H.; Riekkola, M. L. Fluorescein Isothiocyanate Stability in Different Solvents. *Monatshefte fur Chemie* **2021**, *152* (11), 1299–1306. https://doi.org/10.1007/s00706-021-02852-1.

(45) Ardejani, M. S.; Ling Chok, X.; Jin Foo, C.; Orner, B. P. Complete Shift of Ferritin Oligomerization toward Nanocage Assembly via Engineered Protein-Protein Interactions. *Chem. Commun.* **2013**, *49* (34), 3528–3530. https://doi.org/10.1039/c3cc40886h.

(46) Choi, J.; Fuentes, C.; Fransson, J.; Wahlgren, M.; Nilsson, L. Separation and Zeta-Potential Determination of Proteins and Their Oligomers Using Electrical Asymmetrical Flow Field-Flow Fractionation (EAF4). *J. Chromatogr. A* **2020**, *1633*, 461625. https://doi.org/10.1016/j.chroma.2020.461625.

(47) Cummings, E. B.; Singh, A. K. Dielectrophoresis in Microchips Containing Arrays of Insulating Posts: Theoretical and Experimental Results. *Anal. Chem.* **2003**, *75* (18), 4724–4731. https://doi.org/10.1021/ac0340612.

(48) Camacho-Alanis, F.; Gan, L.; Ros, A. Transitioning Streaming to Trapping in DC Insulator-Based Dielectrophoresis for Biomolecules. *Sensors Actuators, B Chem.* **2012**, *173*, 668–675. https://doi.org/10.1016/j.snb.2012.07.080.